Deformation, fracture, and fatigue crack growth behavior in TiB-reinforced near-α Ti matrix composites fabricated using powder metallurgy technique

Qiang Li [a b], Sheng Huang [b], Yimin Gao [a], Upadrasta Ramamurty [b c]

[a]

State Key Laboratory for Mechanical Behavior of Materials, School of Materials Science and Engineering, Xi'an Jiaotong University, Xi'an, 710049, PR China

[b]

School of Mechanical and Aerospace Engineering, Nanyang Technological University, Singapore, 639798, Republic of Singapore

[c]

Institute of Materials Research Engineering (IMRE), Agency for Science, Technology and Research (A*STAR), Singapore, 138634, Republic of Singapore

Abstract

Titanium matrix composites with TA15 alloy as the matrix and TiB (ranging from 0 to 4 vol%) as reinforcement were produced via powder metallurgy-based hot press sintering, employing AlB_2 precursor. The addition of TiB to TA15 led to a substantial reduction in the colony and prior β grain sizes, and an increase in the lath thickness in the composites. Plastic deformation due to planar slip, which traverses across the α/β-ligament phase boundaries within each colony, may cause TiB particles located on colony boundaries to break, potentially more so than those within the colony. The composite containing 1 vol% TiB exhibited simultaneous improvements in strength, ductility, and strain hardening rate, attributed to colony refinement and possibly a sizable amount of intra-boundary TiB. Further increase in the TiB content led to significant drops in ductility, which was further exacerbated by the precipitation of α_2-Ti_3Al phase. A substantial decrease in the mode I fracture toughness, attributed to reduced colony size and diminished crack deflection, was noted in the composite with 1 vol% TiB. The colony size refinement also contributed to a reduction in the threshold stress intensity factor range, ΔK_0, for the fatigue crack growth, owing to the decreased tortuosity of the fatigue crack front. This study elucidates the intricate relationship between TiB location, microstructure, and mechanical properties, providing insights for the design of TiB-reinforced titanium alloys with both α and β phases.

Keywords

Metal matrix composites

Mechanical properties

Fatigue crack growth

Fracture toughness

Titanium alloys

1. Introduction

Titanium and its alloys find extensive applications in the aerospace, chemical, marine, and biomedical industries due to their exceptional mechanical and physical properties, including high specific stiffness and strength at both ambient and elevated temperatures, as well as excellent corrosion and oxidation resistances [1]. In order to enhance their specific strength and service temperature further, titanium matrix composites (TMCs) with various ceramic reinforcements are being explored [[2], [3], [4], [5], [6]]. Amongst them, TMCs with TiB (and TiC) are the most widely studied [3,[7], [8], [9], [10], [11], [12], [13], [14], [15], [16], [17], [18]]. In addition to a high elastic

modulus (~450–550 GPa) [19,20] and melting point (~2200 °C) [21], the similarity in the thermal expansion coefficients of TiB and Ti (CTE_{Ti} = 8.6 × 10^{-6} K^{-1}, CTE_{TiB} = 7.2 × 10^{-6} K^{-1}) [3,22] and the lattice constants (lattice mismatch <3.6 %) are the reasons for TiB being a favorite reinforcement candidate among researchers in this field [23,24]. While increasing the TiB content can lead to significant strength improvements at room temperature (to ~1500 MPa [25,26]) and elevated temperatures (to ~900 MPa at 600 °C [27]), a marked reduction in room temperature ductility often accompanies them, with most TiB/Ti-6Al-4V composites exhibiting elongation to failure of less than 6 % [26]. Overcoming this strength-ductility trade-off in TMCs is a major challenge and, if accomplished, would enhance the overall reliability of this material. Amongst various approaches being explored, refinement of the TiB size or engineering mesostructures through the inhomogeneous distribution of particles show promise [7,[26], [27], [28]]. While such methods have shown improvements in the composite's ductility, they still fall well-short of the ductility of the original monolithic matrix [26,27]. Processing the TMCs with the powder metallurgy routes provides additional flexibility, in terms of controlling the size and spatial distribution of the TiB particles [26,29,30]. Moreover, powder metallurgy is a near-net shape process involving mainly solid-state diffusion [31], which gives it an edge over casting procedures by minimizing the requirement of post-process machining and avoiding solidification defects such as shrinkage pores [30]. It is also important to note that the solidification sequence during casting inherently leads to reinforcement segregation at prior beta grain boundaries [32] —a critical factor known to contribute to premature reinforcement failure [33].

A recent work on La_2O_3/Mo composites suggests that incorporating nano-sized reinforcement particles within the grain, rather than at the grain boundary, can lead to simultaneous enhancements of strength and ductility [34]. Our previous work on TiB/Ti further demonstrates that this concept can be extended to microscale reinforcement particles [35]. By having TiB particles to be within the grain, strain hardening capacity of the alloy is improved by promoting duplex slip, unlike TiB particles in contact with grain boundaries which fail prematurely (and, thus, lead to lower ductility) [35]. This results in simultaneous enhancements of strength, ductility, and fracture toughness, compared to unreinforced commercially pure titanium (CP-Ti) [35].

While the above approach is promising, exploring it in the context of dual-phase Ti alloys (referring to near-α Ti alloys and (α+β) Ti alloys, containing <10 vol% and 5–40 vol% β-Ti phase, respectively [36,37]) is essential, as they are more relevant and widely used as structural materials [38]. The grain boundary structure in CP-Ti is much more simplistic than that in the dual-phase Ti alloys [39,40]. In the latter, one should consider the location of TiB on different types of boundaries, such as α/β phase, colony, and prior β-grain boundaries [[40], [41], [42]]. Therefore, it is imperative to investigate whether the same tactic to introduce the majority of TiB into the grain interior in CP-Ti, as in our previous work [35], will still work on a dual-phase Ti alloy. This is particularly important given that further and extensive formation of α/β-ligament phase boundaries can occur as the alloy cools down [40], thereby increasing the probability of having TiB particles in contact with the phase boundaries, especially when the length of TiB approaches or exceeds that of the α phase. Note that the term α/β-ligament boundary is used instead of α/β boundary to exclude phase boundaries located on the colony boundaries.

Note that whether a TiB particle fails prematurely or not is highly dependent on the slip systems around it. Premature failure of TiB located on a grain boundary could be due to the bending moment induced by multiple slip on different sides of TiB, originating from different grains with different crystallographic orientations [35]. However, TiB within a grain that experiences the same slip systems

around it will have a stress state closer to pure shear, as most Ti alloys possess the planar slip deformation characteristic [[43], [44], [45]]. Given the small misorientation of slip planes between the α phase and β ligaments, slip can pass through their interface with little resistance and have a similar orientation [43,46], rendering the boundary inconsequential for dictating the premature failure of TiB particles. In other words, it could be possible that there is a need to only consider whether TiB is on the colony boundary, as opposed to other boundary types.

In light of the above considerations, we examine the TA15 alloy (a type of near alpha titanium alloy with the nominal composition of Ti-6.5 A l-1Mo-1V-2Zr) reinforced with TiB particles, produced using the powder metallurgy approach with AlB_2 as the precursor. (This method, as mentioned previously, was employed in TiB/Ti TMCs to introduce a majority of TiB into the grain rather than the grain boundary of CP-Ti, although the exact reason for this phenomenon remains unclear [35]). TA15 is known for its elevated temperature properties [47], and reinforcing it with TiB can further enhance these characteristics [48]. However, reinforcements may also reduce its damage tolerance at room temperature, which is crucial for reliable deployment. Therefore, while acknowledging the importance of high temperature usage, this study primarily focuses on the microstructural features and the uniaxial tensile, fracture toughness, and fatigue crack growth behaviors specifically at room temperature. The significance of TiB's interaction with different boundary types and the mechanical behavior associated with different TiB content levels (ranging between 0 and 4 vol%) were investigated. Additionally, a detailed comparison of fracture toughness between the TiB/TA15 composites and TiB/Ti systems [35] was provided.

2. Materials and experiments

2.1. Materials

The metallic matrix of the TMCs is TA15 alloy, a near-α type titanium alloy with the nominal composition of 5.5–7.1 wt% Al, 1.5–2.5 wt% Zr, 0.8–2.5 wt% V, and 0.5–2.0 wt% Mo [49,50]. The raw materials for creating TiB/TA15 consisted of a blend of pre-alloyed TA15 ELI spherical gas atomized powder (median particle size ~100 μm) and fine AlB_2 precursor (>99.5 % purity, <5 μm average diameter). The *in-situ* reaction between AlB_2 and Ti takes place during sintering ($AlB_2 + 2Ti \rightarrow 2TiB + Al$), resulting in the formation of TiB, as well documented in Refs. [18,51]. The fabricated TiB/TA15 composites, with the expected volume fractions of TiB (V_{TiB}%) of 0, 1, 2, and 4 %, are denoted hereafter as A0, A1, A2, and A4, respectively. Their chemical compositions were determined using inductively coupled plasma optical emission spectroscopy (ICP-OES) and are listed in Table 1.

Table 1. Weight of AlB_2 utilized for fabricating samples A0, A1, A2 and A4, along with the estimated TiB volume fractions in them and the measured chemical compositions.

Samples	**Volume fraction of TiB, V_{TiB}%**	**Chemical composition (wt%)**						**AlB_2 content (wt%)**
		Al	**Zr**	**Mo**	**V**	**B**	**Ti**	
A0	0	6.10	1.51	1.04	1.83	–	Bal.	0
A1	1	6.37	1.47	0.91	1.62	0.19	Bal.	0.43
A2	2	6.41	1.53	0.66	1.40	0.38	Bal.	0.85
A4	4	6.92	1.52	1.04	1.66	0.82	Bal.	1.70

The sample fabrication procedure involves ball milling of the powders, followed by hot-press sintering. Predefined proportions of TA15 and AlB_2 powders were first mixed and then subjected to planetary

ball milling with agate milling balls inside a stainless-steel jar under an argon atmosphere. Each powder batch undergoes a total milling time of 8 h, with a rotation speed of 150 rpm and a ball-to-powder ratio of 5:1. The primary purpose of the ball milling process is to uniformly coat the relatively large TA15 particles with the AlB_2 particle satellites. Negligible changes in particle size and morphology can be seen after milling, as shown in Fig. S1. Subsequently, the milled powder is transferred to a columniform graphite mold and subjected to reaction-sintering using a hot-press sintering system operating under a high vacuum (10^{-3} Pa). An initial 30-min degassing procedure at 250 °C was conducted, followed by powder consolidation at 1200 °C for 60 min under 20 MPa pressure, and then furnace cooling. The procedure resulted in 45 mm (diameter) × 18 mm (height) cylindrical samples with virtually negligible porosity, which were inspected through optical microscopy of the polished cross-sections.

2.2. Experiments

The specimens for microstructural characterization were subjected to mirror polishing using successively finer SiC papers, followed by 3 μm diamond and 0.04 μm SiO_2 + H_2O_2 suspensions. The addition of H_2O_2 facilitates the removal of surface residual stress and improves EBSD pattern quality, which is a chemical-mechanical polishing approach commonly employed for metallography preparation of titanium and its alloys [[52], [53], [54]]. When necessary, they were also etched with the Kroll's reagent. Subsequently, they were examined using a scanning electron microscope (SEM) equipped with the detectors for energy-dispersive X-ray spectroscopy (EDS) and electron backscatter diffraction (EBSD). The EBSD mapping was conducted with a maximum step size of 0.5 μm. Various microstructural parameters, such as the volume fractions of TiB (V_{TiB}%), the width of the α-phase lamellae (λ), and the colony size (μ_D, equivalent circle diameter) were obtained by analyzing the SEM images that were obtained under the backscatter electron (BSE) mode, covering an area of ~0.88 mm^2, and the EBSD maps generated over an area of ~2.8 mm^2. A colony in an α/β titanium alloy refers to a microstructural region where the α phase and β phase are oriented in a specific, repeating pattern, embedded within the prior β phase. The α lamellae within a colony share a common crystallographic orientation, which differentiates them from adjacent colonies that have different orientations [40,55,56]. The EBSD analyses also facilitate the retrieval of information on the prior β grain size (d_β) through parent grain reconstruction procedure that was based on the orientation relationship of $(110)_{\beta\text{-}Ti}//(0002)_{\alpha\text{-}Ti}$ [57].

Uniaxial tensile testing on specimens with the dimensions of 6 mm (gauge length), 2 mm (width), and 1 mm (thickness) was performed with a universal testing machine (UTM) equipped with a laser extensometer [[58], [59], [60]]. The tests were conducted at a nominal strain rate of 10^{-3} s^{-1} following the ASTM-E8 standard [61]. Five tests were conducted for each case of A0 – A4.

The fracture toughness and fatigue crack growth (FCG) tests were conducted on a servo-hydraulic universal testing machine (MTS 810), as per the ASTM E399-20a [62] and E647-15 [63] standards, respectively. At least two chevron-notched compact tension (C(T)) specimens of 12 mm thickness (B) and 24 mm width (W) were tested for each TMC [64,65]. Prior to the fracture toughness tests, the C(T) specimens were mirror polished on both the sides and fatigue pre-cracked until the a/W ratio is within 0.45–0.55 (a is the crack length). A 10 Hz sinusoidal wave load with a load ratio of 0.1 was applied for FCG; the crack length was tracked with a long-distance high-resolution optical microscope capable of 60X magnification. Pre-cracked specimens were quasi-statically pulled at a constant crosshead speed of 0.002 mm/s to obtain fracture toughness values based on the ASTM E399-20a standard [62]. If the ligament size (W - a) is large than $2.5(K_Q/\sigma_y)^2$, the mode I fracture toughness, K_{IC}, was obtained;

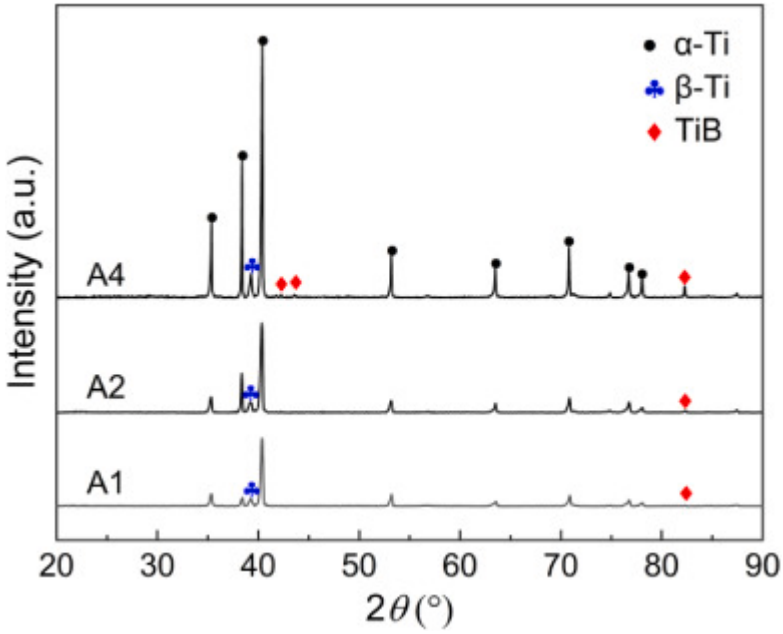
otherwise, the conditional fracture toughness, K_Q, was obtained. Post-mortem analyses were conducted on the polished side surfaces of the C(T) specimens using SEM and EBSD, where the specimens were sliced from the middle of the thickness to understand the crack behavior in the plane strain condition, where necessary.

The values of threshold stress intensity factor range (ΔK_o) were identified based on the load shedding method that was prescribed in the ASTM 647-15 standard [63]. The stress intensity factor range (ΔK) was decreased by ~2 % after every ~200 μm of crack growth, upon which the ΔK is defined as ΔK_o when the crack growth rate (da/dN) reaches below $\sim 2 \times 10^{-10}$ m/cycle. The Paris's law, $da/dN = C\,(\Delta K)^m$ was then fitted against the values of da/dN vs. ΔK for each specimen in the steady-state crack growth regime to estimate the Paris constant, C and Paris exponent, m. The side and fracture surfaces of the C(T) specimens were characterized with SEM and EBSD to understand the interaction of the cracks with the microstructural features.

3. Results

3.1. Microstructures

Results of the XRD experiments, performed on A1–A4 samples to reveal the phase compositions of TiB/TA15 composites, are shown in Fig. 1. The diffraction peaks in A1–A4 indicate the presence of α-Ti (hexagonal close-packed), β-Ti (body-centered cubic), and TiB (orthorhombic) phases, indicating the near complete dissociation and reaction of AlB_2 powder with Ti, consistent with previous investigations on the TiB/Ti composites [35,66].

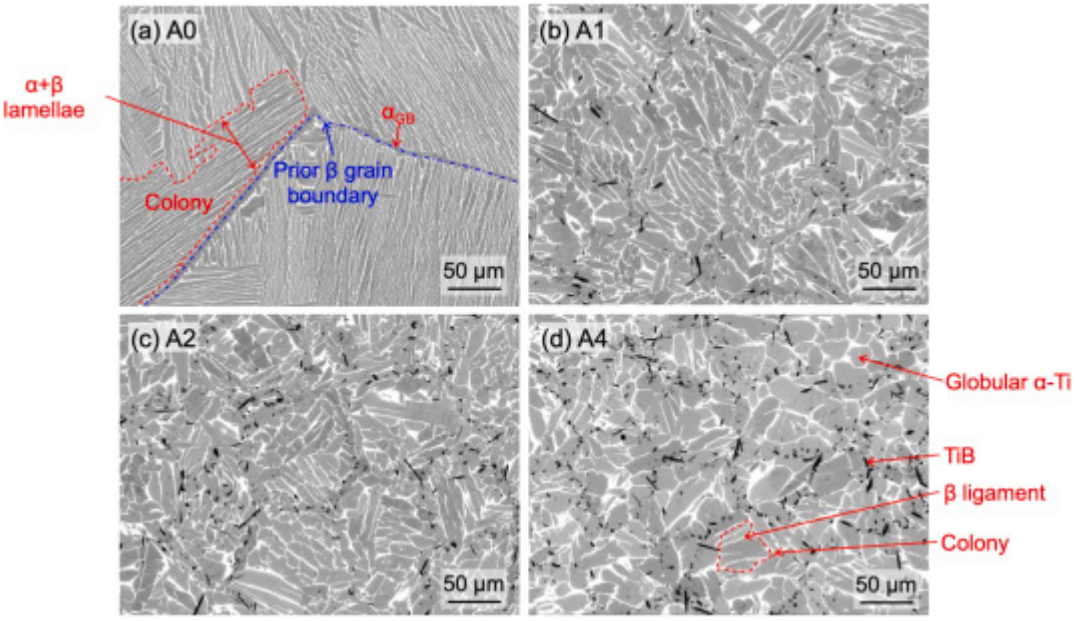


1. Download: Download high-res image (229KB)
2. Download: Download full-size image

Fig. 1. XRD analysis of A1–A4 samples.

To investigate the evolution of microstructure with increasing TiB content, backscatter electron (BSE) images of A0–A4 samples were obtained, as shown in Fig. 2. When TiB is absent, the A0 sample exhibits the α + β lamellae colony microstructure, with clearly distinguishable large prior beta grains (~782.2 μm), along with grain boundary α (α_{GB}) that forms along the prior β grain boundaries. The large prior beta grain size, in comparison to the powder size (~100 μm), can be attributed to significant grain growth during sintering and has been observed in previous literatures [67,68]. This microstructure is

typical of α+β Ti alloys, commonly observed in slow-cooled castings and PM products [69]. With the presence of TiB in A1–A4, α_{GB} could not be found, and the morphology of α-Ti changes to oval-shaped or globularized, as shown in Fig. 2b–d. The TiB particles in A1 – A4 are distributed in a 'necklace' fashion highlighted in Fig. S2, which has been widely reported in TiB/TMCs fabricated using the PM and casting approaches [32,[70], [71], [72]]. This phenomenon arises from the tendency of TiB to form at the prior powder surface and retain their positions even after sintering and densification. It is important to note that, the prior β grain boundary can grow beyond the surface of the powder particle upon sintering, leading to some TiB particles not being in contact with the colony boundaries. This is supported by previous work on TiB/Ti, where the grain can grow beyond the typical necklace structure, even when the TiB content is 6 vol% [66].

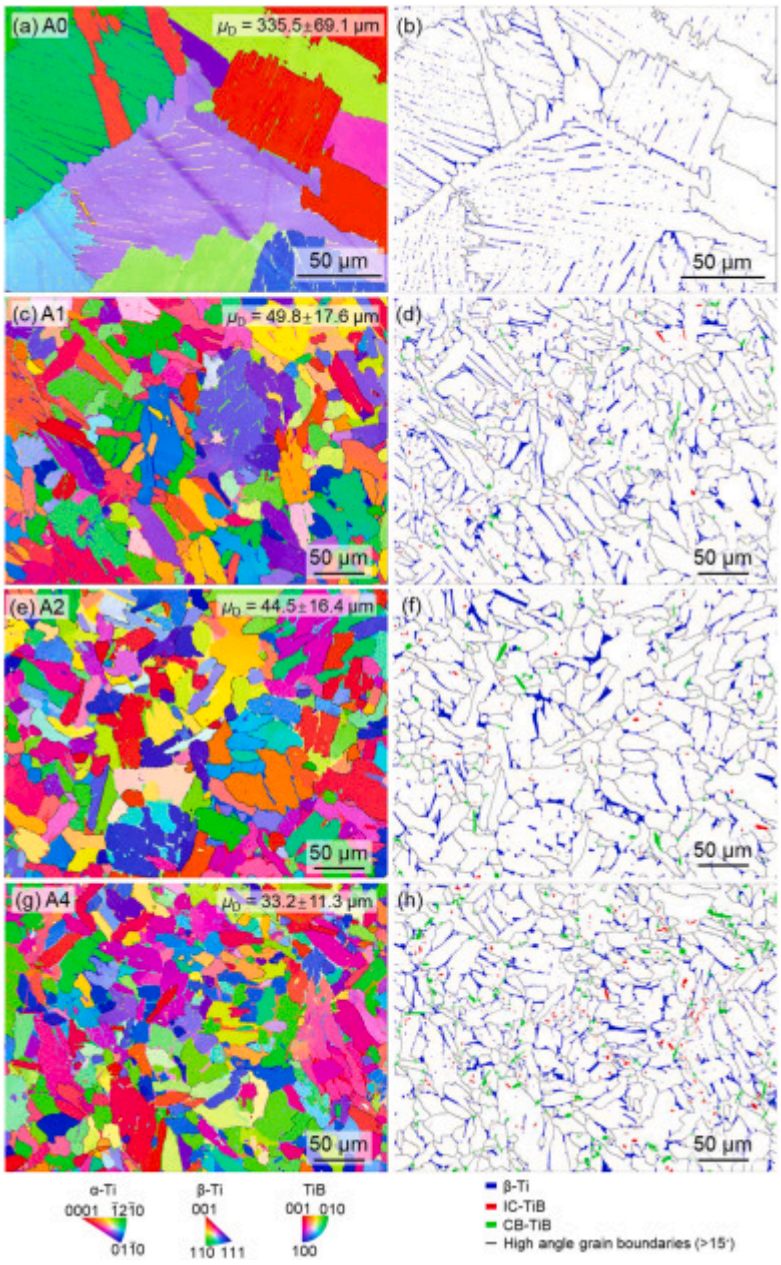


1. Download: Download high-res image (826KB)
2. Download: Download full-size image

Fig. 2. Representative microstructure for (a) A0, (b) A1, (c) A2, and (d) A4 samples. The bright, grey, and dark phases are β-Ti, α-Ti, and TiB phases, respectively.

In our prior work on the TiB/Ti composites, we have shown that the location of TiB within the Ti matrix, whether in contact with the grain boundary or within the grain, greatly affects the mechanical properties [35]. When situated at the grain boundaries (GBs), it tends to promote easy cracking, whereas when located within the grain, it promotes strain hardening, thereby enhancing ductility. The α+β Ti (e.g., TA15), as opposed to α titanium (e.g., CP-Ti), has a considerably more complex microstructure [43], wherein additional boundaries such as α/β-ligament phase, colony, and prior β boundaries need to be considered, as illustrated in Fig. 2, to understand the mechanical response. In view of this, EBSD analysis was conducted over an area of approximately ~2.8 mm^2 on the samples to assist in quantifying the location of TiB, with representative EBSD results shown in Fig. 3. The phase maps with the reconstructed prior β boundaries are given in Fig. S3, with the reconstruction operation based upon the Burgers' relationship of $\{110\}_{\beta\text{-}Ti}//(0002)_{\alpha\text{-}Ti}$, $[1\,\bar{1}\,1]//[11\bar{2}\,0]$ [57]. For a simple and yet meaningful approach to categorize the location of TiB in such a complex microstructure, the following two important points must be noted. 1) Based on our previous work, a beneficial trait of TiB in improving strain hardening is observed when slip traces of similar direction surround the TiB particle [35]. 2) For the α+β titanium, it is well known that slip can be fairly easily transferred across the α/β-

ligament phase boundaries within an α/β colony [73], where μ_D in an alloy with fully lamellar microstructure dictates the effective slip length [41]. With this basis, TiB particles that are within the colonies (including those on the α/β-ligament phase boundaries) are categorized as one type, referred to as 'Inner Colony TiB' (IC-TiB) hereafter. Note that the colony can be identified with the aid of EBSD as a region of the α phase having the same orientation (the β ligaments between the α phases are also part of the colony), hence the same inverse pole figure (IPF) color. Those in contact with the colony boundary (which also include the prior β grain boundaries) are referred to as 'Colony Boundary TiB' (CB-TiB). The volume fractions (*V*%) of IC- and CB-TiB (TiB%) are carefully measured and tabulated in Table 2. While a sizable amount of TiB is situated within the colony boundaries (~40 %) for A1–A4, the use of AlB_2 precursor did not lead to a majority of TiB being within the grain boundary, unlike our previous study on TiB/Ti (>70 %) [35]. It is also important to note that the percentage value here may be underestimated, as the analysis was performed on 2D cross-sections, with the possibility of TiB being in contact with the colony boundary but not visible on the analyzed slice. Nevertheless, the data is representative of the trend in IC-TiB and CB-TiB vol% as TiB content varies. To support this, additional statistical analysis was performed by counting the number of points where TiB is in contact with the CB-TiB boundaries, normalized by the investigated area, to directly quantify the density of such potential weak points without the influence of TiB size. The results are shown in Table S1. It was found that this metric correlates well with the value of CB-TiB vol%, as shown in Fig. S4.



1. Download: Download high-res image (2MB)
2. Download: Download full-size image

Fig. 3. Representative EBSD analysis of (a, b) A0, (c, d) A1, (e, f) A2, and (g, h) A4: (a, c, e, g) Grain orientation maps with IPF coloring, (b, d, f, h) Phase maps showing IC-TiB and CB-TiB, colored in red and green, respectively. (For interpretation of the references to color in this figure legend, the reader is referred to the Web version of this article.)

Table 2. Summary of the microstructural parameters for A0–A4 samples.

Empty Cell	$V_{TiB,\ total}$%	μ_D (μm)	d_β (μm)	λ (μm)	TiB_{CB}%	TiB_{IC}%	$V_{CB\text{-}TiB}$%	$V_{IC\text{-}TiB}$%
A0	0	335.5 ± 69.1	782.2 ± 161.3	3.5 ± 0.2	–	–	–	–
A1	1	49.8 ± 17.6	93.5 ± 36.3	12.3 ± 0.5	59.8 ± 9.1	40.2 ± 9.1	0.59 ± 0.09	0.41 ± 0.09

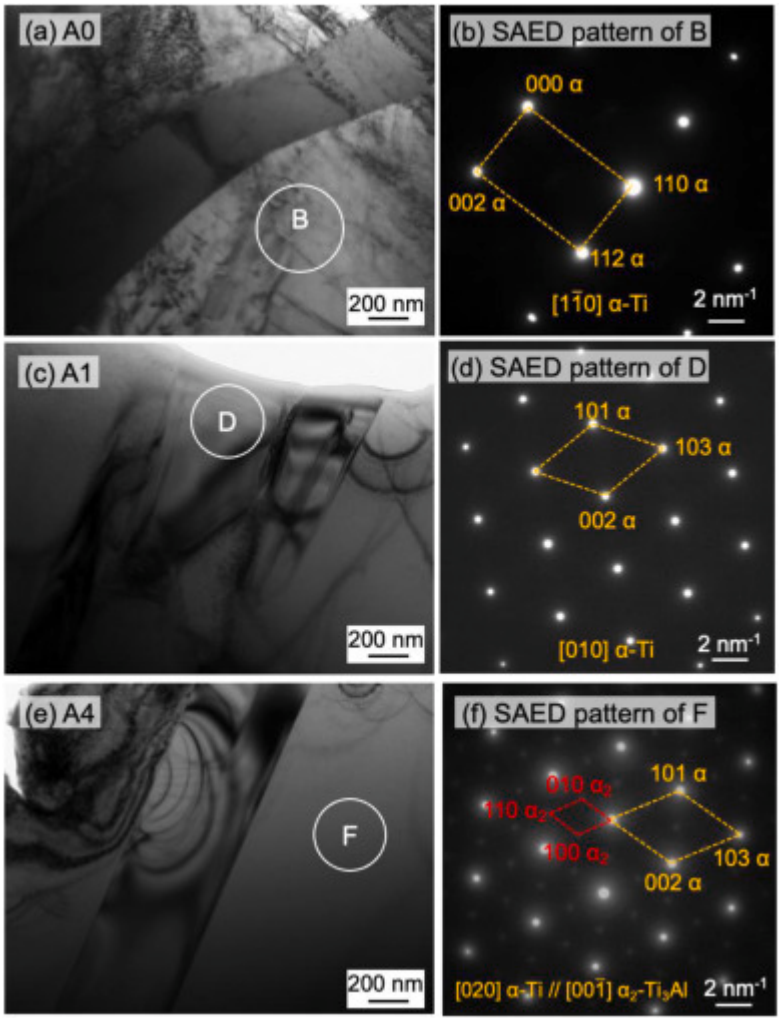
Empty Cell	$V_{TiB,\ total}$%	μ_D (μm)	d_β (μm)	λ (μm)	TiB_{CB}%	TiB_{IC}%	$V_{CB\text{-}TiB}$%	$V_{IC\text{-}TiB}$%
A2	2	44.5 ± 16.4	84.3 ± 22.9	11.3 ± 0.5	59.4 ± 9.2	40.6 ± 15.5	1.24 ± 0.42	0.76 ± 0.42
A4	4	33.2 ± 11.3	76.4 ± 20.2	14.5 ± 0.5	64.9 ± 3.9	35.1 ± 3.9	2.60 ± 0.37	1.40 ± 0.37

Using the EBSD analysis with Aztec Crystal software, the width of α-phase lamellae (λ), colony size (μ_D) and prior β grain size (d_β) were obtained and listed in Table 2. With the presence of TiB, both μ_D and d_β decrease, while λ increases markedly. The significant reductions in both μ_D (from ~355.5 μm in A0 to ~49.8 μm in A4) and d_β (from ~782.2 μm in A0 to ~93.5 μm in A4) are attributed to the ability of TiB to pin prior β grains and heterogeneously nucleate α-Ti [[74], [75], [76]]. The grain refinement (i.e., reduction in μ_D and d_β) with further addition of TiB is not significant, due to the saturation of the growth restriction factor [32,76]. The reason behind the increase in λ with the TiB addition (from ~3.5 μm in A0 to ~12.3 μm in A1), however, is not understood yet, despite it being consistently observed in many prior studies on as-cast TiB/Ti64 composites [1].

The precipitation of the α_2-Ti_3Al phase, an intermetallic with the $D0_{19}$ crystal structure, which typically strengthens the alloy while simultaneously embrittling it, is widely reported in the near-α Ti alloys when the solubility limit of Al (7 wt%) is exceeded [15,77,78]. Given the high level of Al in the matrix (6 wt%), the possibility of α_2 precipitation in the present TiB/TA15 samples due to the usage of AlB_2 precursor needs to be examined. Hence, EDS measurements were performed on all samples to reveal the composition variation caused by the increasing AlB_2 addition, as shown in Table 3. It was found that the Al concentration of α phase in A4 indeed exceeded the 7 wt% threshold for α_2 phase formation. Its existence in A4 and absence in other specimens are further confirmed by TEM analysis, shown in Fig. 4, where the SAED patterns of TiB and the α phase in A4 are accompanied by that of α_2 (High resolution TEM analysis for the α_2 phase in A4 is given in Fig. S5). The absence of α_2 in A0 and A1 is also shown in Fig. 4.

Table 3. Chemical compositions of α- and β-Ti phases in A0–A4 samples measured by EDS.

Phases	**Samples**	**Chemical compositions (wt%)**				
		Al	**Zr**	**Mo**	**V**	**Ti**
α-Ti	A0	6.08 ± 0.15	1.83 ± 0.13	–	1.20 ± 0.16	Bal.
	A1	6.78 ± 0.05	1.65 ± 0.06	–	1.13 ± 0.10	Bal.
	A2	6.85 ± 0.17	1.75 ± 0.13	–	1.15 ± 0.13	Bal.
	A4	7.25 ± 0.13	1.73 ± 0.05	–	1.08 ± 0.10	Bal.
β-Ti	A0	3.25 ± 0.21	2.53 ± 0.10	6.35 ± 0.26	6.40 ± 0.36	Bal.
	A1	3.43 ± 0.10	2.78 ± 0.15	7.45 ± 0.61	7.48 ± 0.40	Bal.
	A2	3.60 ± 0.12	2.83 ± 0.21	7.45 ± 0.51	8.05 ± 0.19	Bal.
	A4	4.28 ± 0.22	2.78 ± 0.15	7.53 ± 0.79	7.45 ± 0.24	Bal.

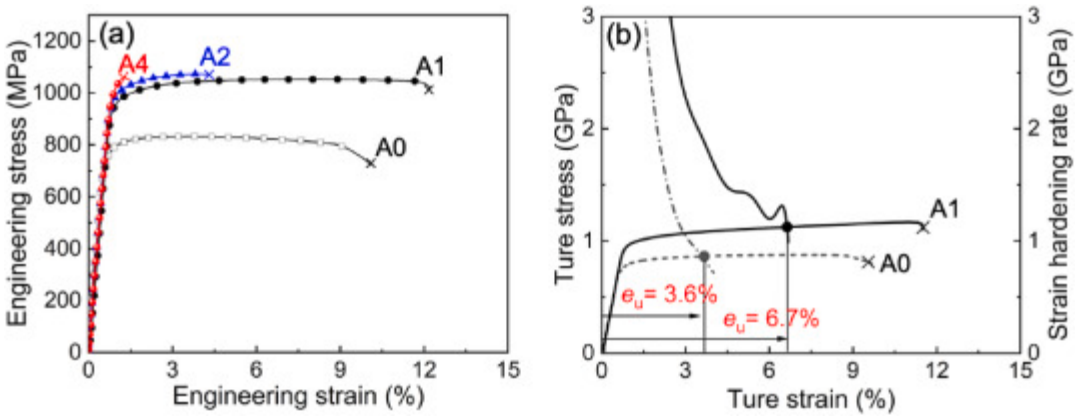


1. Download: Download high-res image (581KB)
2. Download: Download full-size image

Fig. 4. Representative TEM analyses of (a, b) A0, (c, d) A1, and (e, f) A4 samples: (a, c, e) Bright-field TEM images of A0, A1, and A4 samples, respectively, and (b, d, f) SAED patterns from areas around the α-Ti phase in A0, A1, and A4, aimed at investigating the presence of the α_2 phase.

3.2. Uniaxial tensile properties

Fig. 5a presents the representative engineering stress-strain responses obtained from the A1–A4 samples, and Fig. S6 displays all the engineering stress-strain responses obtained. The values of the yield strength (σ_y), ultimate tensile strength (σ_u), uniform elongation (e_u), elongation to failure (e_f), and strain hardening capacity ($\sigma_u - \sigma_y$) are summarized in Table 4. Values of e_u were obtained using the Considère's criterion for the onset of necking, as illustrated in Fig. 5b.



1. Download: Download high-res image (289KB)
2. Download: Download full-size image

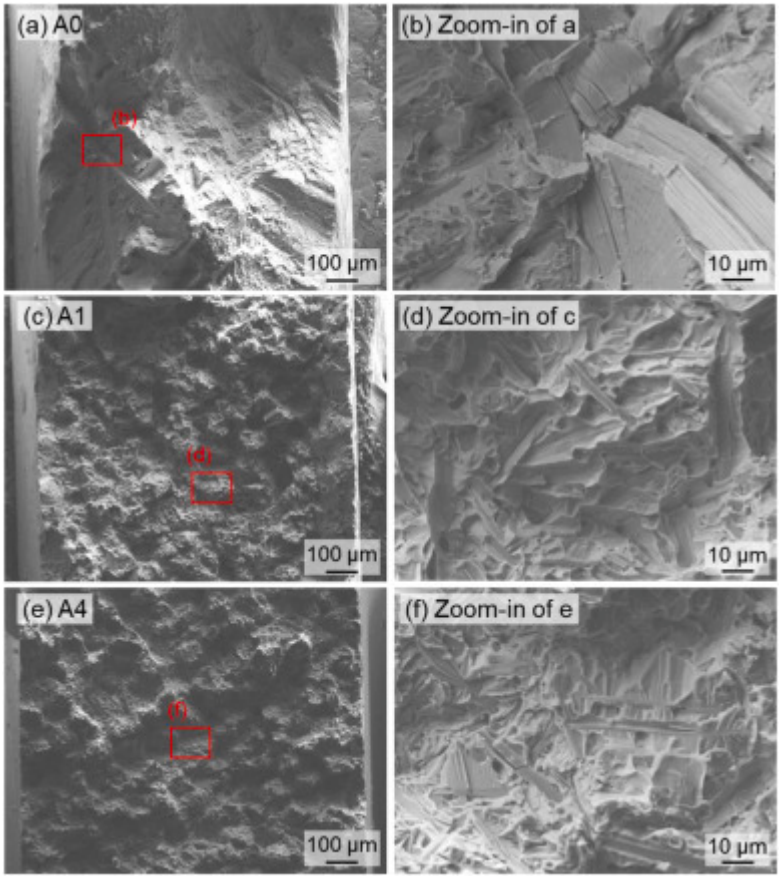
Fig. 5. Representative uniaxial tensile behaviors: (a) representative engineering stress-strain curves of A0–A4; (b) The representative true stress-strain curves vs. corresponding SHR curves of A0 and A1.

Table 4. Summary of the uniaxial tensile properties.

Empty Cell	σ_y(MPa)	σ_u (MPa)	e_u (%)	e_f (%)	$\sigma_u - \sigma_y$ (MPa)
A0	810 ± 20	850 ± 15	3.8 ± 0.8	8.2 ± 2.0	39 ± 7
A1	967 ± 9	1047 ± 7	6.9 ± 1.0	9.7 ± 2.0	81 ± 10
A2	995 ± 13	1071 ± 7	3.5 ± 0.8	3.9 ± 0.9	76 ± 11
A4	–	1033 ± 27	–	1.0 ± 0.2	–

The σ_y, σ_u, and e_f of the as-sintered TA15 alloy (A0) in this work are measured as 810 and 850 MPa, and 8.2 %, respectively. Upon the addition of 1 vol% TiB, simultaneous enhancements in strength and ductility were observed, with σ_y ~967 MPa, σ_u ~1047 MPa, and e_f ~9.7 %, which are 19.4 %, 23.2 %, and 18.3 % improvements, respectively, compared to A0. An 81.6 % improvement in uniform elongation (e_u), from ~3.8 % to 6.9 %, was also noted; this can be attributed to the additional strain hardening capacity (($\sigma_u - \sigma_y$) ~39 MPa for A0 and ~81 MPa for A1). Note that the σ_y and e_f of the as-sintered TiB/TA15 composites, reported in the literature, are within the ranges of 941–1144 MPa and 1.7–7.3 % [51,[79], [80], [81]], respectively, as shown in Table S2. However, with further addition of TiB, only a ~28 MPa improvement of σ_y from A1 to A2 is observed at the expense of the e_f dropping significantly from 9.7 % to 3.9 %; the A4 sample containing 4 vol% TiB exhibits a brittle behavior with little or no plasticity beyond yield, with a e_f of 1.0 % and σ_u of 1033 MPa.

Fractographic images shown in Fig. 6 reveal marked differences in the fracture features of the samples with and without TiB. The fracture surface of A0 exhibits large cleavage facets, while A1–A4 display finer fracture features. These differences are consistent with the microstructural features' size or the colony size (μ_D). Despite the improvement of ductility from A0 to A1, dimples are sparsely observed in the A1 sample, indicating the lack of micronecking prior to fracture. Hence, it can be surmised that plasticity in this composite is uniform elongation dominated. This is further exemplified by the observation that the ductile A1 exhibits fracture features akin to those of the brittle A2 and A4.



1. Download: Download high-res image (720KB)
2. Download: Download full-size image

Fig. 6. Representative fracture morphologies of tensile-tested specimens for A0, A1, and A4: (a, c, e) show the overall fracture surfaces, while (b, d, f) provide magnified views of features from (a, c, e), respectively, highlighting detailed fracture characteristics.

3.3. Fracture toughness

Mode Ⅰ fracture toughness, K_{IC}, was experimentally evaluated using the C(T) specimens based on the ASTM E399 standard [62], and the results are tabulated in Table 5. All the samples satisfy the plane strain conditions stipulated in the ASTM standard E399 [62], with the exception of the TA15 alloy (A0 in this study), with the two measured fracture toughness values of 90.0 and 100.6 MPa$\sqrt{m}$. Consequently, those are designated as K_Q. Nevertheless, they can be deemed as being close to K_{IC}, as the largest estimated plane strain plastic zone size in A0 (~1.5 mm) is only about one-eighth of B and exhibits near elastic-perfectly plastic deformation characteristics (similar justifications made in previous studies on TiB/Ti TMC [35], Ti-6Al-4V [64,82], and Ti34Nb [52]). Furthermore, the K_Q values of TA15 or A0 obtained in this study are well within the previously reported K_{IC} values, which range between 74 and 140 MPa$\sqrt{m}$ [49]. This gives us further confidence in the cross comparison of the fracture toughness values of A0 and A1–A4. With 1 vol % TiB content, the observed drastic 64.3 % drop in fracture toughness value from 95.3 MPa$\sqrt{m}$ (A0's average toughness) to 34.0 MPa$\sqrt{m}$ (A1) is rather intriguing, considering the simultaneous improvements in strength and ductility (relative to A0). Although the fracture toughness dropped considerably (compared to the matrix alloy), it is comparable to that reported Ti64 with a similar d_β [1,83]. Further TiB addition leads to K_{IC} reduction from A2 (28.0 MPa$\sqrt{m}$) to A4 (20.5 MPa$\sqrt{m}$), consistent with the embrittlement behavior seen during the uniaxial tensile tests. The drastic deterioration of fracture toughness

observed from A0 to A1 will be further discussed in a later section.

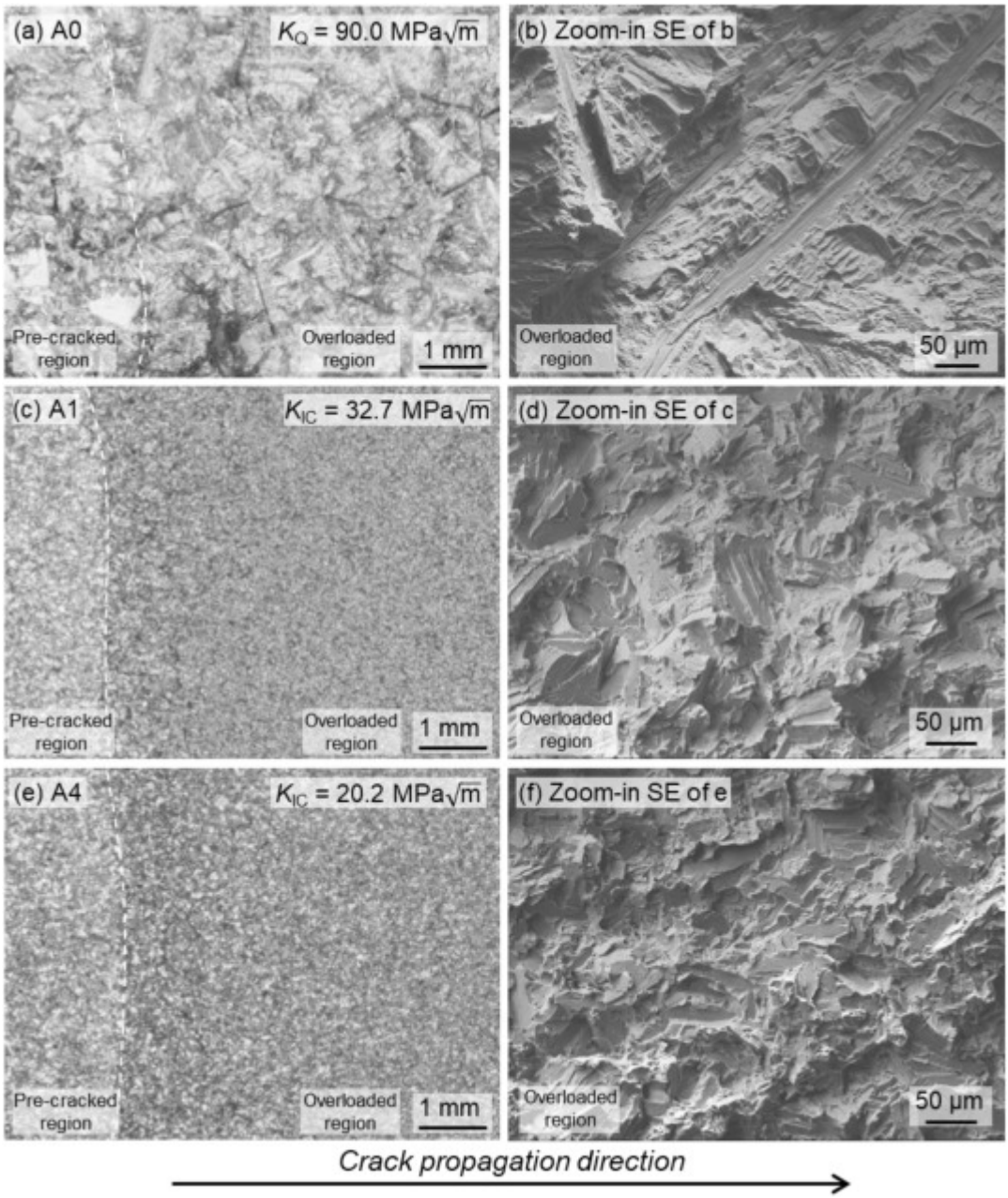
Table 5. Summary of fracture toughness and FCG properties. The data in parentheses indicate the values obtained from the individual experiments.

Empty Cell	K_{IC} (MPa m)	ΔK_o (MPa m)	m	ΔK_T associated with μ_D (MPa m)
A0	95.3[a] (90.0[a], 100.6[a])	9.4 (9.4, 9.3)	4.4 (4.7, 4.0)	91.1
A1	34.0 (32.7, 35.3)	5.3 (5.1, 5.5)	5.0 (4.8, 5.1)	41.9
A2	28.0 (27.4, 28.5)	5.6 (5.8, 5.4)	5.4 (5.3, 5.4)	40.8
A4	20.5 (20.2, 20.7)	5.5 (5.5, 5.4)	5.5 (5.4, 5.5)	36.5

a

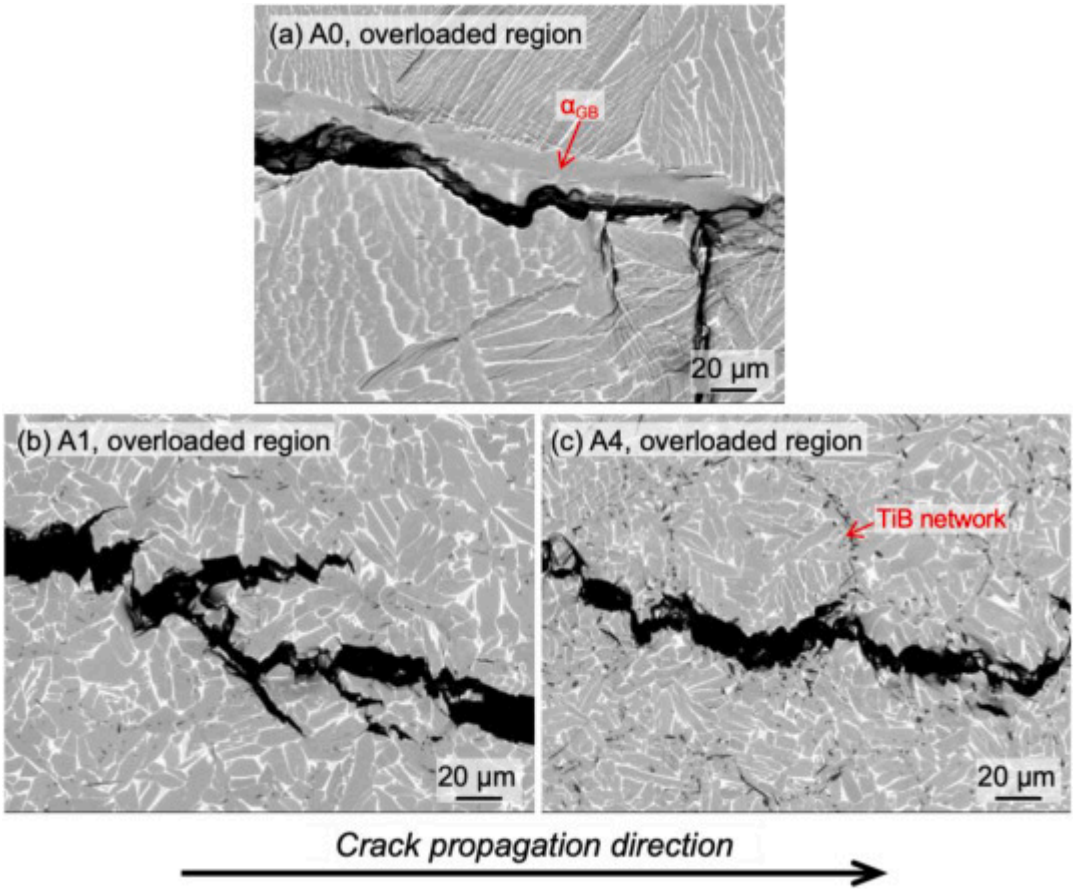
Plane strain conditions are not satisfied as per ASTM E399-20a, hence are designated as K_Q.

Fig. 7 shows the SEM fractographs obtained from the "overload regions" of the fracture surfaces in the fractured A0–A4 specimens. Similar to those observed in the uniaxial tensile test, the fractographs displayed in Fig. 7a and b show large cleavage facets in A0 compared to A1–A4 (Fig. 7b–d). Moreover, the large cleavage facets result in a rough fracture surface, suggesting their correlation to the increased resistance to crack propagation, via enhanced crack tortuosity, in A0. An examination of the side surfaces of the C(T) specimens in the overload crack propagation region (Fig. 8) reveals that with the continuous TiB necklace structure, which becomes more apparent with the increasing TiB content, provides an easy path for unstable crack propagation [35]. In addition, crack propagation along the grain boundary α (α_{GB}) can be observed in the overload fractured region of A0, as shown in Fig. 8a. Despite the observed poorer fracture toughness performance at room temperature, the inclusion of 1 vol% TiB proves beneficial in enhancing both the strength and ductility of TA15, warranting future investigation into its performance at elevated temperatures, which we plan on undertaking in future.



1. Download: Download high-res image (1MB)
2. Download: Download full-size image

Fig. 7. Fractographs obtained on the overload fractured regions of the (a, b) A0, (c, d) A1, and (e, f) A4 specimens. The representative OM fractographs are shown in (a, c, e), while the respective zoom-in SE images of the overload region are displayed in (d–f).

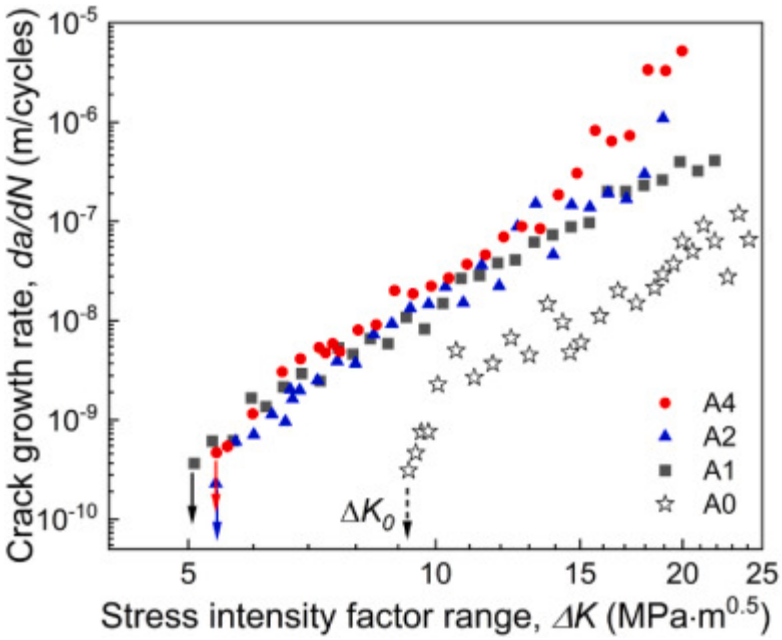


1. Download: Download high-res image (728KB)
2. Download: Download full-size image

Fig. 8. Representative side view of the overload fracture regions for A0, A1, and A4 specimens, as captured under BSE imaging mode.

3.4. Fatigue crack growth

The effect of TiB content on the fatigue crack growth (FCG) behavior of A0–A4 samples was investigated, and the representative FCG curves are shown in Fig. 9. From this data, the empirical Paris equation, $da/dN = C(\Delta K)^m$ that relates the crack growth rate (da/dN) to ΔK, was utilized, where C and m are material constants that are often referred to as Paris constant and Paris exponent, respectively. Values of the threshold stress intensity factor range, ΔK_0, and m, for the A0–A4 samples obtained from the FCG curves are listed in Table 5. The FCG behavior in the TMCs with and without TiB present a stark contrast, with A0 exhibiting a significantly slower FCG rate than all the other (A1–A4) samples. Incidentally, A1–A4 show nearly-identical FCG responses at the threshold and steady-state FCG regions. The only difference is that A4 shows accelerated fast crack growth as the maximum stress intensity of the fatigue cycle approaches its fracture toughness.

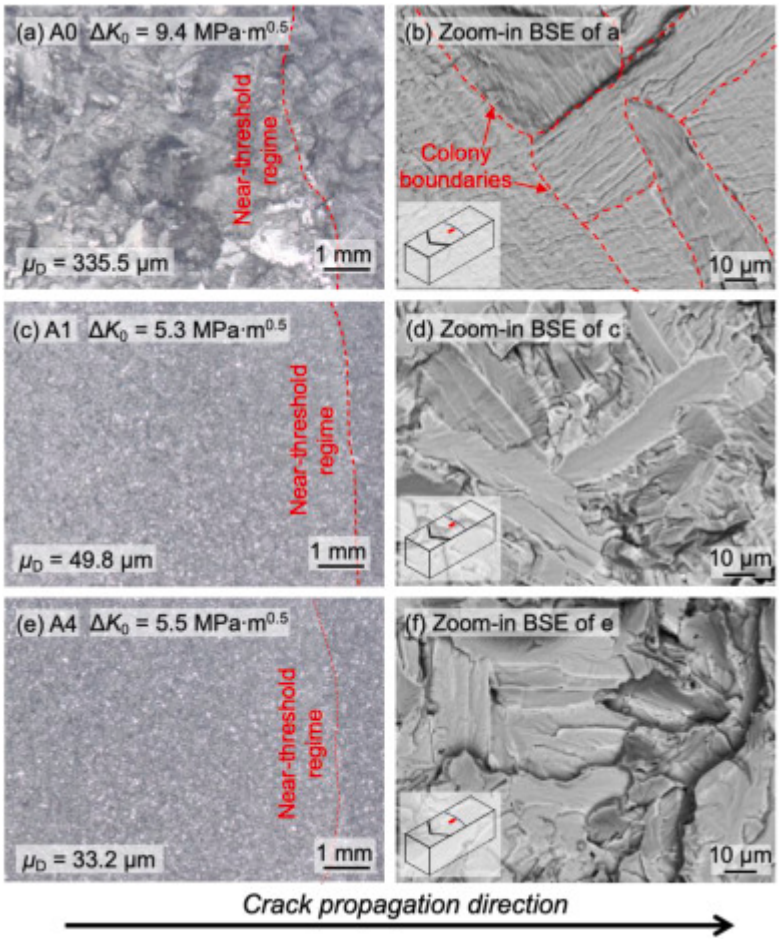


1. Download: Download high-res image (309KB)
2. Download: Download full-size image

Fig. 9. Representative FCG behaviors for A0–A4 samples. Upon reaching d*a*/d*N* value ~2 × 10^{-10} m/cycles, the corresponding ΔK_0 can be determined.

The average ΔK_0 measured in A0 is 9.4 MPa$\sqrt{m}$. The addition of 1 vol% TiB led to a 43.6 % reduction in ΔK_0 to 5.3 MPa$\sqrt{m}$. A further increase in the TiB content to 2 and 4 vol% had only a marginal effect on ΔK_0, with average ΔK_0 values of 5.6 and 5.5 MPa$\sqrt{m}$, respectively. The addition of TiB also led to an deleterious effect on the Paris exponent as well, with the *m* values increasing from 4.4 to 5.5 from A0 to A4, signifying an acceleration in the crack growth rate in the 'steady state regime' as the crack grows longer.

The FCG surfaces of all samples were also investigated and presented in Fig. 10. Similar to the fractographs of monotonically loaded and fractured samples, the FCG surface of A0 is highly tortuous compared to samples with TiB. Fractography, performed under the BSE imaging mode, reveals that the fatigue fractured facet is closely related to the colonies. Fatigue striations are also absent in all the samples, suggesting that the damage accumulation model of FCG (which predicts $m = 4$), as opposed to the geometrical model (that results in $m = 2$) [[84], [85], [86]], is better suited to describe fatigue crack propagation in TA15. Additional factors have to be considered when *m* deviates further from 4 with the TiB addition.



1. Download: Download high-res image (905KB)
2. Download: Download full-size image

Fig. 10. Representative fractographs of the fatigue cracked region for (a, b) A0, (c, d) A1, and (e, f) A4. (a, c, e) provide overviews, while (b, d, f) show zoomed-in views under BSE imaging mode, focused near the fatigue threshold region. These detailed images emphasize the relationship between fracture features and colony size. The ΔK_0 and average colony size (μ_D) are annotated on the corresponding images.

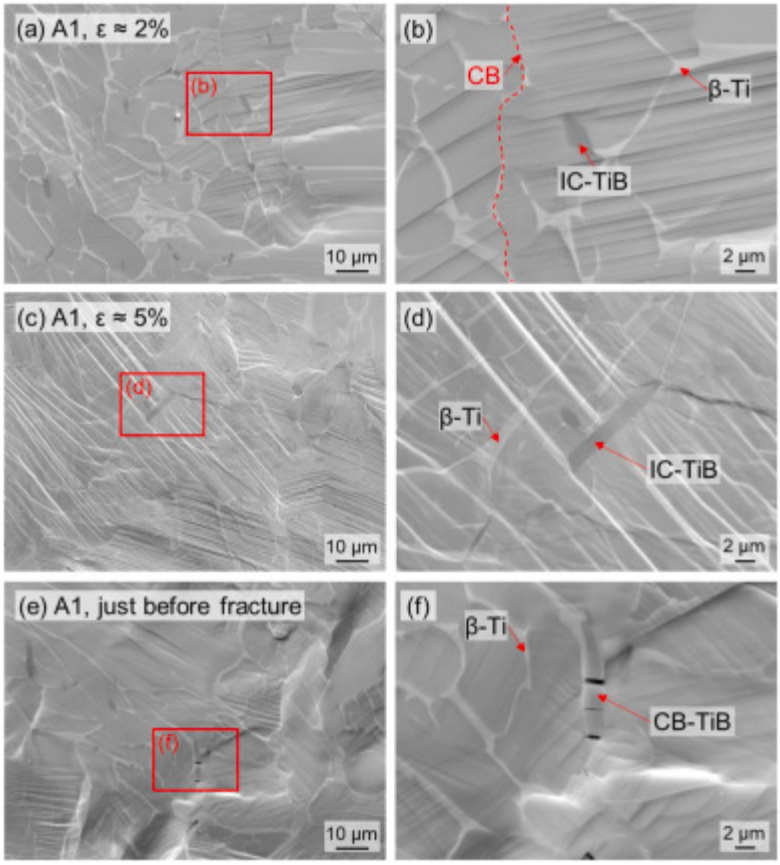
4. Discussion

4.1. The critical role of TiB's location within the microstructure

In our previous research on TiB/Ti (which possesses a single α-Ti phase matrix) [35], we demonstrated that locating TiB within the α-Ti grain, rather than at the α-Ti grain boundary, is advantageous for enhancing strain hardening. This occurs through the promotion of the duplex and wavy slip by TiB. Conversely, TiB present at the grain boundaries, influenced by different slip planes in neighboring grains, has the potential to induce bending moments rather than pure shear (as observed for TiB within a grain), thereby increasing its fracture susceptibility, which, in turn, lowers the overall ductility of the alloy.

With the above understanding, we investigated the effect of TiB's location at different regions of the dual phase (α+β) TA15 alloy, specifically in the A1 sample. However, the complexity of this investigation is compounded by the need to consider the impact of α/β phase boundaries. To address this, interrupted tensile tests were conducted at various strain levels (2 %, 5 %, and just before fracture) to observe the formation of slip and the roles of IC-TiB and CB-TiB, as illustrated in Fig. 11. A

micrograph of A1 at 5 % strain showing the slip lines and the corresponding EBSD analysis is also provided in Fig. S7, to highlight the role of colony boundaries in constricting slip transfer.



1. Download: Download high-res image (621KB)
2. Download: Download full-size image

Fig. 11. SEM analysis of the A1 sample's surface (free surface) during an interrupted tensile test at various strains: (a, c, e) depict the surface at 2 %, 5 %, and just before fracture, respectively. Images (b, d, f) offer higher magnification views of (a, c, e), respectively, highlighting the interactions of slip traces with TiB and the state of TiB (whether broken or unbroken).

Up to a strain of 5 % (before the sample necks), planar slip dominates, as seen in Fig. 11(a–d), with slip traces consistently observed to remain within a single colony and, then, while penetrating through the α/β phase boundary. These observations are consistent with those reported in literature on the α+β Ti alloys [41,43,46]. However, unlike the TiB/Ti composites [35], IC-TiB did not facilitate the formation of duplex and wavy slip in the TiB/TA15 composites. This observation suggests that IC-TiB's contribution to strain hardening may not be as significant as that reported in single phase Ti (i.e., CP-Ti). Instead, the benefits of TiB addition primarily arise from strength enhancement through load sharing and grain refinement in the α/β matrix [66,70]. Refinement of colony size is known to simultaneously enhance strength and ductility in the α+β titanium alloys [1,22]. A comparison of data available in literature for the hot-pressed TA15 shows that a higher σ_y ~900 MPa and e_f ~20 % were obtained with a prior β grain size of ~100 μm [8], as opposed to the results in our study with a grain size of ~700 μm (σ_y ~810 MPa and e_f ~8.2 %). This is attributed to the alloy's intrinsic propensity for planar slip and the increased presence of grain boundaries facilitating strain delocalization and distribution. Upon straining prior to fracture, as observed in Fig. 11(e and f), CB-TiB exhibited a higher propensity for fracture compared to IC-TiB, which tended to remain intact. Given the similar fraction

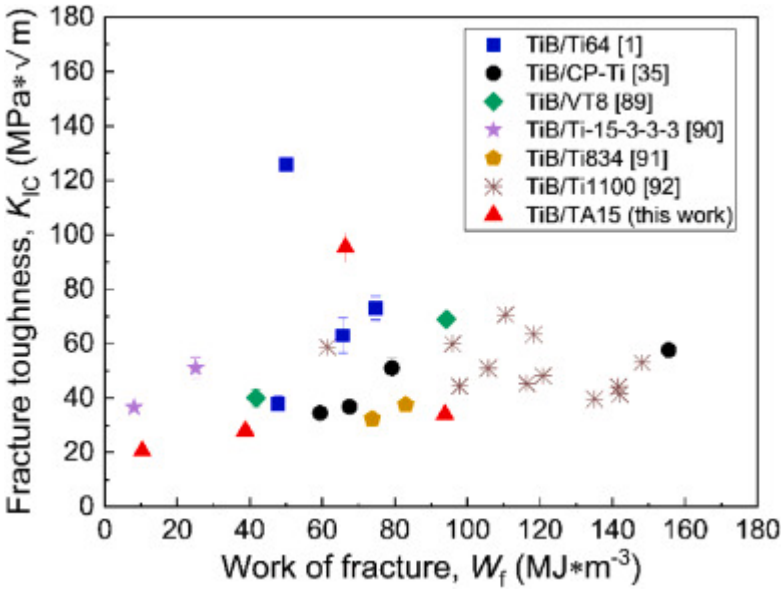
of IC-TiB (~40 %) relative to CB-TiB in all the TMCs of this study, an increase in the overall TiB content meant a greater absolute number of TiB particles with a higher tendency to fracture, which deteriorates the tensile ductility.

In summary, while the microstructure can become quite complicated when the α/β phase boundary is involved, our hypothesis is that the problem of determining the better location of TiB can be resolved by simply considering deformation slip. Since slip traces penetrate even the α/β phase boundary, when they are within a colony, the location of TiB, regardless of whether it is on the α/β boundary or not, appears to be not an issue. This simplifies the problem by only requiring identification of whether TiB is on the colony boundary or not. This means that increasing the IC-TiB fraction is crucial for delaying fracture and improving the ductility of the TiB/TA15 TMC, similar to what was previously learnt on the TiB/Ti system [35]. It is good to note that as the TiB particles are randomly oriented in this study, the effect of loading direction with respect to TiB's orientation is not explored. A future study focusing on manufacturing composites with highly aligned TiB particles would be beneficial to systematically examine the effect of loading direction and the tendency to break. To develop a comprehensive understanding of the interactions between different TiB types and dislocations, work involving focused ion beam lift-outs of interrupted tensile-tested specimens for transmission electron microscopy analysis can be performed in future. This approach is essential to isolate the effect of grain orientation, allowing for the selection of different TiB types (CB- vs. IC-TiB) located in similar grain orientations and neighboring orientations for observation at different strain levels. Additionally, this method will enable the selection of TiBs with similar alignment to isolate their potential effect on dislocation interaction. By conducting such an investigation, damage nucleation from a dislocation interaction perspective can be probed in detail.

It is also important to note that there is currently no clear understanding of the nucleation and growth of TiB particles from the AlB_2 precursor, and significant uncertainty exists regarding the precise location of TiB based solely on 2D analysis. As a result, the claim regarding IC- vs. GB-TiB in this study, especially when the particle size is similar to that of individual grains, remains a sound hypothesis rather than an established fact. The IC- vs. GB-TiB classification and their associated findings warrants further investigation to determine the accuracy of this classification and its exact impact on mechanical properties.

4.2. Fracture toughness

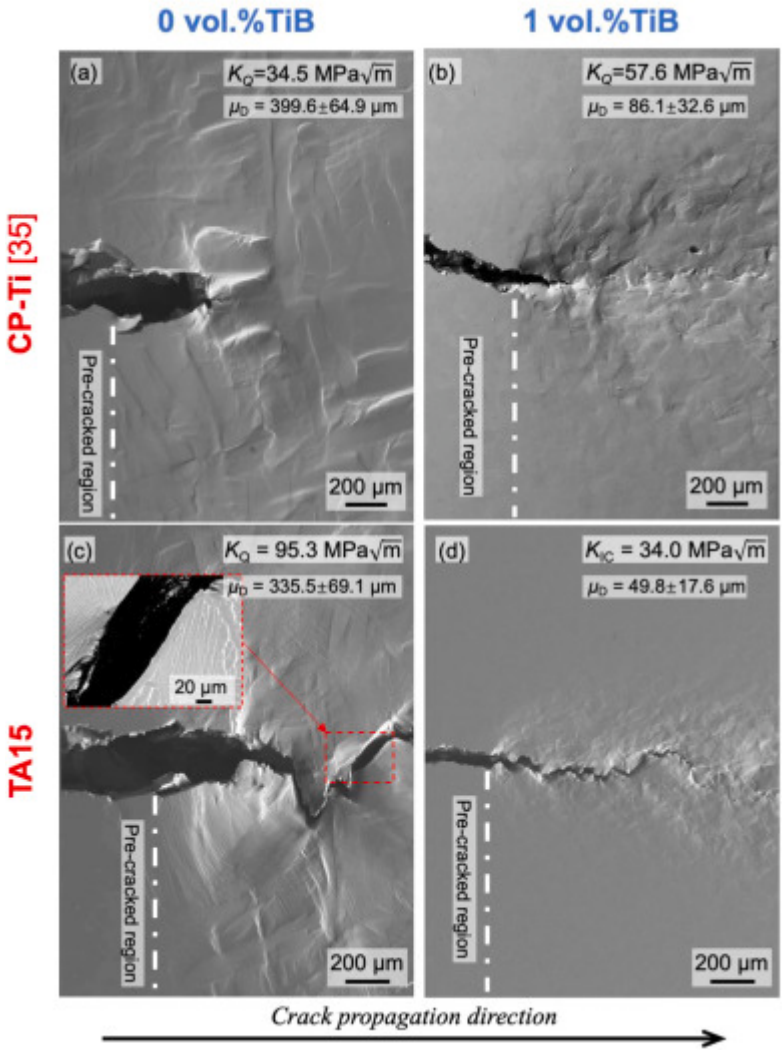
Despite the well-established strength-toughness trade-off [87], many researchers working in this area still attempt to correlate ductility improvement with a potential fracture toughness enhancement [88], especially since uniaxial tensile tests are easier to perform and straightforward to interpret. With this in mind, we collected data from previous literature on TiB/TMCs [1,35,[89], [90], [91], [92]] which included both tensile and fracture toughness data. We then plotted the experimental K_{IC} values against the area under the tensile stress-strain responses, which can be considered as the work of fracture (W_f), in Fig. 12. A lack of correlation between these properties is obvious.



1. Download: Download high-res image (293KB)
2. Download: Download full-size image

Fig. 12. Fracture toughness versus work of fracture data reported in literature for TiB reinforced TMCs, illustrating the lack of correlation between these parameters [1,35,[89], [90], [91], [92]].

Upon the addition of 1 vol% TiB to the alloy, a marked reduction in K_{IC} was observed, despite simultaneous improvements in both σ_y and e_u. This is in complete contrast with the observations of our previous study on TiB/Ti [35], which demonstrated simultaneous enhancements in strength, ductility, and fracture initiation toughness for a similar increase in the TiB volume fraction. Observations made on the side surface, immediately ahead of the crack tip, reveal that the A0 sample exhibits substantial (~200 μm) crack deflection along the grain boundary α phase (Fig. 13c), a phenomenon that was also noted in literature [1,49]. Crack deflection to such an extent was not observed in the A1 sample, see Fig. 13d. These features are in complete contrast to those made on TiB/Ti in our prior work, as illustrated in Fig. 13. While Ti with 1 vol% TiB exhibits crack tortuosity similar to that of TA15 with 1 vol % TiB in this study, CP-Ti (without any TiB addition) shows a straight crack, as seen in Fig. 13a [35]. Crack deflection serves as an extrinsic toughening mechanism by diverting cracks from mode I propagation, thus significantly reducing the driving force for crack propagation for the same far-field stress intensity factor [53,[93], [94], [95]]. The reduced extent of crack deflection justifies the drop in the fracture toughness of TA15 due to the suppression of extrinsic toughening upon 1 vol% TiB addition.



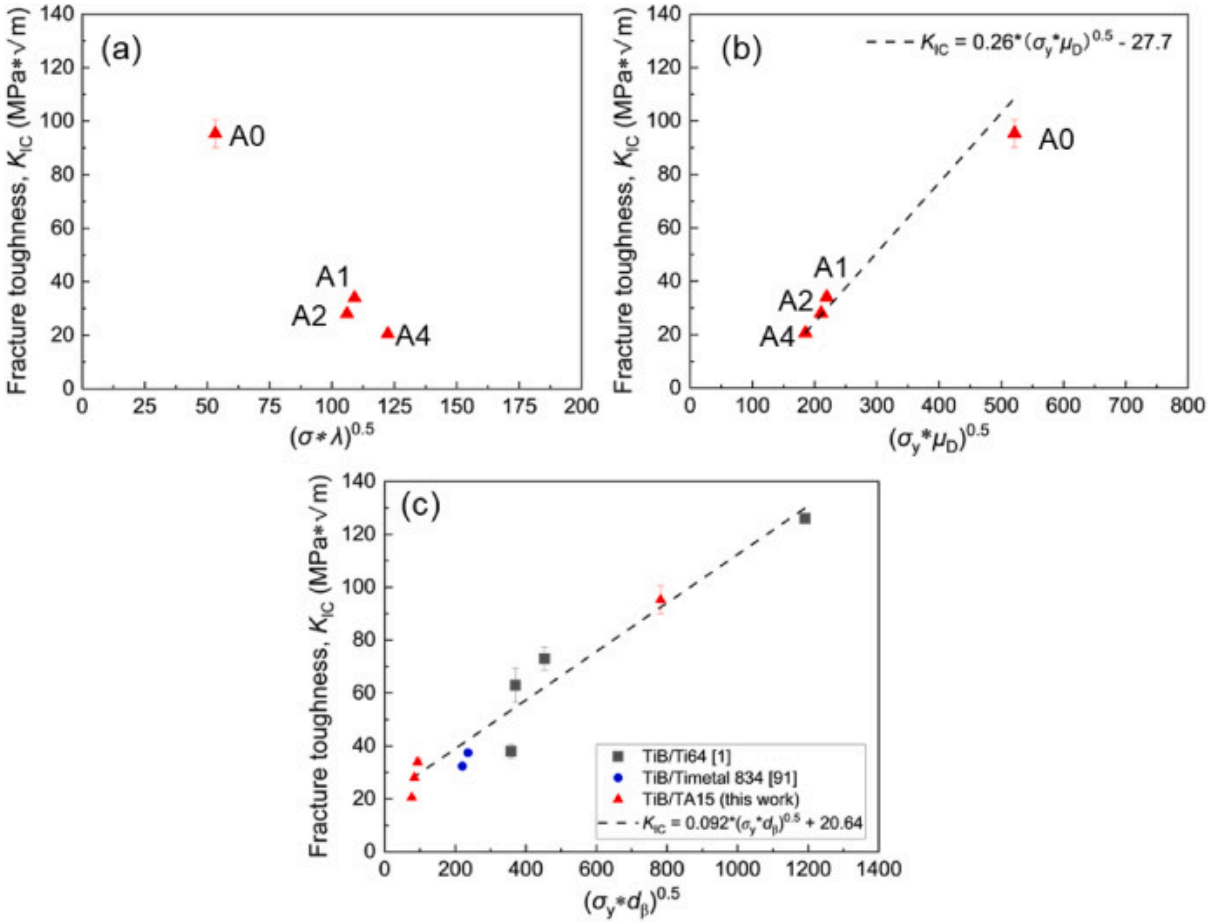
1. Download: Download high-res image (656KB)
2. Download: Download full-size image

Fig. 13. Representative side views (plane-stress) of the cracked C(T) samples' surfaces: (a) CP-Ti [35] and (b) 1 vol% TiB reinforced CP-Ti [35], followed by (c) A0 (the insert image shows crack propagates along the α_{GB}) and (d) A1 samples.

The Ritchie–Knott–Rice (RKR) model can also be applied to correlate the microstructural effect on the fracture toughness in TiB/TA15. This model postulates a criterion for cleavage initiation ahead of sharp cracks, stating that the local tensile stress must surpass a critical fracture stress (σ_f) over a microstructurally significant length scale ($l*$) for fracture to initiate [96,97]. This model has been used to predict how cleavage fracture toughness changes with temperature in mild steel and has found application across various types of steels, titanium alloys, and boron-modified titanium alloys [1,22,96,97]. By employing the RKR criterion (and assuming that the alloys under consideration do not strain harden, which is reasonable given that most Ti alloys exhibit (nearly) elastic-perfectly plastic response), the following relation between fracture toughness and characteristic length scale can be arrived at [1]:(1)KIC∼l∗σy.

The variations in K_{IC} with $\sqrt{(l*\sigma_y)}$ are plotted, by taking the lath width (λ), colony size (μ_D), and prior beta-grain size (d_β) as $l*$ in Fig. 14a, b, and c, respectively. As μ_D dictates the average slip length, one can see that its usage led to a highly proportional relationship (with high goodness of fit, R^2 ∼0.96)

between the two axis, as shown in Fig. 14b. In contrast, the usage of lath size led to a deviation from the RKR model, as shown in Fig. 14a. Since most prior literature on TMCs provided only d_β and not μ_D, we also attempted the same plot using d_β, as shown in Fig. 14c. We found generally good linear correlation for an aggregate of all data (including the data from literature, showing R^2 ~0.94), though not as good of a fit as using μ_D obtained for TiB/TA15 in this study. While one can argue that d_β is not equal to the characteristic slip length (hence should not be used to verify the RKR model), the addition of boron into α+β Ti alloys tends to refine both α colony and prior-β grain sizes, leading to a certain correlation between the two. Hence, the usage of d_β also appears to comply with the RKR model. However, it is important to note that in a monolithic α+β titanium alloy, such correlation of μ_D and d_β does not always hold true. For instance, a study has shown that d_β can be kept constant while μ_D can be changed by modifying the cooling rate [55].



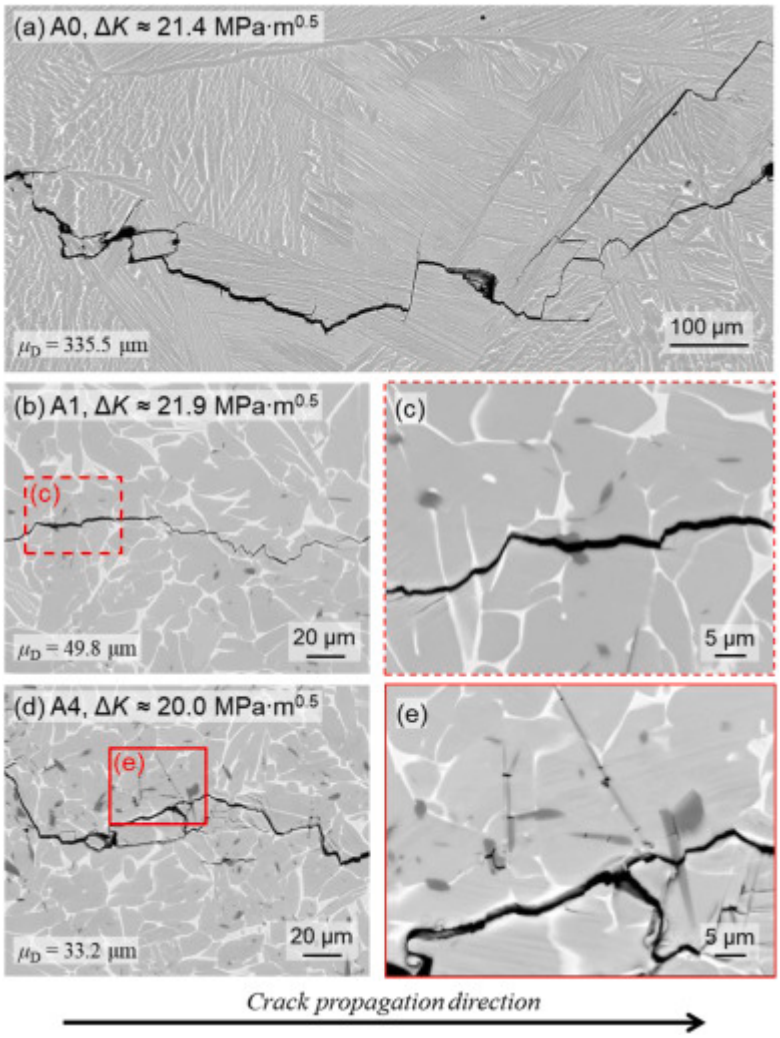
1. Download: Download high-res image (462KB)
2. Download: Download full-size image

Fig. 14. Variation of fracture toughness, K_{IC}, with $(l* \cdot \sigma_y)^{0.5}$ of A0–A4, where $l*$ represents (a) λ, (b) μ_D, and (c) d_β. For (c), data from previous literature on TiB-reinforced α+β Ti alloys were also included [1,91].

4.3. Fatigue crack growth

The observations of FCG surface features in Fig. 10 points toward the correlation of crack deflection with the superior FCG response of A0 and, conversely, the deterioration in the presence of TiB, accompanied by a reduction in the extent of crack tortuosity. Side surface observations on the A0, A1, and A4 specimens that were subjected to FCG experiments (when the applied ΔK is approximately

20 MPa√m), shown in Fig. 15, further highlight the extent of crack deflection in A0 and the absence of such deflections in A1 and A4.



1. Download: Download high-res image (848KB)
2. Download: Download full-size image

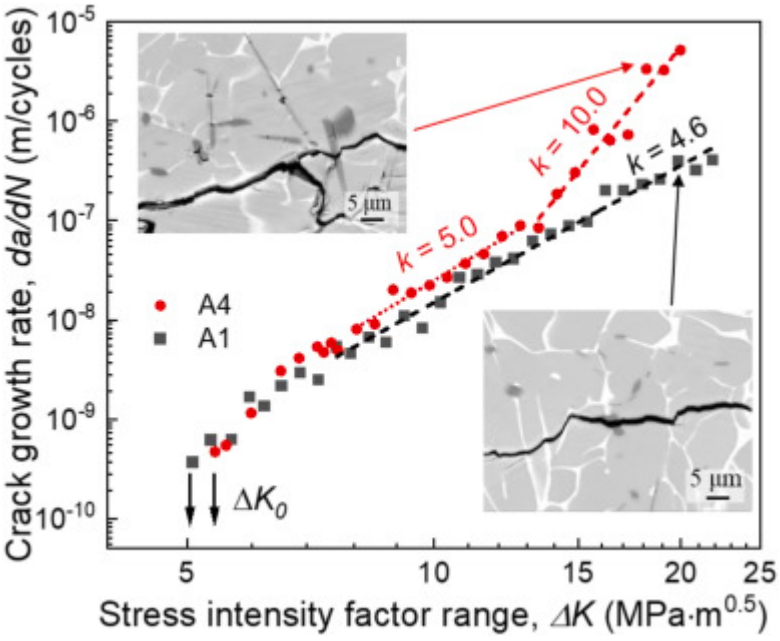
Fig. 15. Representative side views of fatigue cracks in A0, A1, and A4 samples within the higher ΔK region (~20 MPa√m), with (c) and (e) providing zoomed-in views of (b) and (d), respectively.

To explain this, it is imperative to recognize that a transition from microstructure-insensitive to microstructure-sensitive FCG behavior can occur when the cyclic plastic zone size (r_c) becomes comparable to the characteristic microstructural dimension ($l*$) of the material under investigation, i.e., $r_c = 13\pi(\Delta KT2\sigma y)2 \approx l*$ [35,86,98], where $l*$ represents the feature size that encompasses the length of slip (with little resistance and deviation) in metallic materials, such as grain size. In the case of β-annealed Ti-6Al-4V alloys, the Widmanstätten packet size and the colony size (i.e., μ_D) can be taken as $l*$ [41,86,99]. The α/β phase boundaries within a colony offer little resistance to slip [41,43,46]. Hence, the slip traces can be seen traversing an entire colony (see section 4.1). Given that slip precedes fatigue crack growth in α/β Ti, where cracks form along slip traces [86,100,101], colony boundaries play a crucial role in inducing crack deflection, as previously illustrated with Fig. 10, Fig. 15. This observation indicates that the presence of colony boundaries overshadows the role of α/β interfaces within a colony in crack resistance and deflection.

Recognizing this, the transition stress intensity factor ranges, ΔK_T, were calculated based on μ_D for all

samples and listed in Table 5. The range of ΔK employed in this study consistently falls below ΔK_T for all the samples. This observation indicates a microstructure-sensitive FCG response (even in the Paris regime, where it is supposed to be microstructure-insensitive [86]) presented in Fig. 9 [35,86]. This sensitivity leads to observable crack deflection from one colony to another, as previously discussed and illustrated using Fig. 10. Notably, the magnitude of deflection increases with μ_D, resulting in further deviation from mode I crack propagation and a consequent reduction in the driving force for crack growth under the same far-field ΔK. This observation helps rationalize the overall superior performance of FCG exhibited by A0 relative to A1–A4, as μ_D in the former is substantially (nearly-seven times) larger than those of A1 and A2.

It is also noteworthy to briefly discuss the presence of a rapid crack growth region in A4. To illustrate this, Fig. 16 provides separate Paris curves for A1 and A4, facilitating an exclusive comparison between the two. Notably, a significant slope transition (k = 5.0 vs. k = 10) is observed on the FCG curve of A4 at $\Delta K \approx 14$ MPa$\sqrt{m}$, indicating a transition from steady-state to accelerated FCG. In Fig. 15, within the rapid crack growth region for A4, pronounced crack deflection and bifurcation are observed, in contrast to A1, which remains in the steady-state crack growth regime at a similar ΔK. A magnified view of the side surface shown in Fig. 15 depicts the differing condition of TiB around the crack in A1 versus A4. In A1, none of the TiB particles in the vicinity of the crack are broken, except for those in the crack path. In A4, however, many broken TiB particles are found around the crack path. This also means that cracks can initiate from broken TiB particles ahead of the crack tip, leading to a microcracked region that is far ahead of the crack tip; the coalescence such microcracks can facilitate easier macrocracking, thereby providing pathways for crack propagation that result in rapid crack growth. The observed crack bifurcation is a consequence of the multiple easy paths for crack propagation.



1. Download: Download high-res image (325KB)
2. Download: Download full-size image

Fig. 16. Comparison of FCG data between A1 and A4 samples. Insets show representative side-view BSE images in the higher ΔK region (~20 MPa$\sqrt{m}$).

5. Summary

In this study, TiB-reinforced TA15 composites with 0–4 vol% TiB were fabricated via powder-metallurgy-based hot press sintering utilizing an AlB_2 precursor. Detailed microstructural investigations show that the addition of TiB results in a substantial reduction (by nearly an order of magnitude) in the colony and prior β grain sizes, while the average α lamellae's thickness increases; within the TiB added alloys, the variation in these parameters is not significant. During plastic deformation, planar slip that traverses entirely within the colony (without being obstructed by the α/β-ligament phase boundaries) was observed, suggesting that TiB particles in contact with colony boundaries may fail earlier than those within colonies. Composites with 1 vol% TiB exhibited simultaneous enhancements in strength, ductility, and strain hardening, attributed to colony refinement (that aids in a better strain distribution) and the considerable amount of approximately 40 % of TiB not in contact with colony boundaries, which are less susceptible to premature cracking. It is important to note that the accuracy of such a classification of TiB based on contact with colony boundaries requires further investigation, and the associated findings in this study remain a sound hypothesis. However, increasing the TiB content to 2 vol% and 4 vol% resulted in pronounced reduction in ductility, which is further exacerbated by the precipitation of α_2-Ti_3Al phase. Despite improvements in the tensile properties, fracture toughness was observed to drop markedly with the 1 vol% TiB addition to the base alloy. Considering the reduced crack deflection observations upon TiB addition, along with Ritchie–Knott–Rice model analysis, it was revealed that colony size reduction is the primary contributor to the observed loss of fracture toughness. It also led to a reduction in the threshold stress intensity factor range, ΔK_0, during fatigue crack growth owing to the reduced tortuosity of the crack front.

CRediT authorship contribution statement

Qiang Li: Writing – original draft, Visualization, Methodology, Investigation, Conceptualization. **Sheng Huang:** Writing – review & editing, Validation, Supervision, Methodology, Investigation, Conceptualization. **Yimin Gao:** Supervision, Resources, Project administration, Funding acquisition. **Upadrasta Ramamurty:** Writing – review & editing, Supervision, Resources, Project administration, Funding acquisition.

Declaration of competing interest

The authors declare that they have no known competing financial interests or personal relationships that could have appeared to influence the work reported in this paper.

Acknowledgements

The authors acknowledge the financial support from the National Key Research and Development Program of China (2021YFB3701204), the Key-Area Research and Development Program of Guangdong Province (2019B010942001). The work at Nanyang Technological University was supported by Agency for Science, Technology and Research (A∗STAR) of Singapore via the Structural Metal Alloys Programme (No. A18B1b0061). Additionally, the authors would like to extend their appreciation to Mr. Yu Chen for the assistance with sample fabrication.

Appendix A. Supplementary data

The following is the Supplementary data to this article.Download: Download Acrobat PDF file (998KB)

Multimedia component 1.

Data availability

Data will be made available on request.

References

1. [1]

I. Sen, S. Tamirisakandala, D.B. Miracle, U. Ramamurty
Microstructural effects on the mechanical behavior of B-modified Ti-6Al-4V alloys
Acta Mater., 55 (15) (2007), pp. 4983-4993, 10.1016/j.actamat.2007.05.009
View PDFView articleView in ScopusGoogle Scholar

2. [2]

E.T. Zhao, S.C. Sun, Y. Zhang
Recent advances in silicon containing high temperature titanium alloys
J. Mater. Res. Technol., 14 (2021), pp. 3029-3042, 10.1016/j.jmrt.2021.08.117
View PDFView articleView in ScopusGoogle Scholar

3. [3]

M.D. Hayat, H. Singh, Z. He, P. Cao
Titanium metal matrix composites: an overview
Compos Part a-Appl S, 121 (2019), pp. 418-438, 10.1016/j.compositesa.2019.04.005
View PDFView articleView in ScopusGoogle Scholar

4. [4]

P.R. Smith, F.H. Froes
Developments in titanium metal matrix composites
J. Met., 36 (3) (2013), pp. 19-26, 10.1007/bf03338403
Google Scholar

5. [5]

R. Vaidyanathan, D.C. Dunand, U. Ramamurty
Fatigue crack-growth in shape-memory NiTi and NiTi–TiC composites
Materials Science and Engineering: A., 289 (1–2) (2000), pp. 208-216, 10.1016/s0921-5093(00)00882-0
View PDFView articleView in ScopusGoogle Scholar

6. [6]

I. Sen, U. Ramamurty
Elastic modulus of Ti–6Al–4V–xB alloys with B up to 0.55wt
Scr. Mater., 62 (1) (2010), pp. 37-40, 10.1016/j.scriptamat.2009.09.022
View PDFView articleView in ScopusGoogle Scholar

7. [7]

L.J. Huang, L. Geng, H.X. Peng
Microstructurally inhomogeneous composites: is a homogeneous reinforcement distribution optimal?
Prog. Mater. Sci., 71 (2015), pp. 93-168, 10.1016/j.pmatsci.2015.01.002
View PDFView articleView in ScopusGoogle Scholar

8. [8]

Y. Feng, W. Zhang, L. Zeng, G. Cui, W. Chen
Room-temperature and high-temperature tensile mechanical properties of TA15 titanium alloy and TiB whisker-reinforced TA15 matrix composites fabricated by vacuum hot-pressing sintering
Materials, 10 (4) (2017), 10.3390/ma10040424
Google Scholar

9. [9]

R. Zhang, K. Xu, F. Sun, Z. Ma, L. Huang, L. Bolzoni, L. Geng, F. Yang
Achieving highly variable mechanical behaviors in TiBw/TA15(Si) composite by microstructure

manipulation
Mater. Charact., 212 (2024), 10.1016/j.matchar.2024.113978
Google Scholar
10. [10]
Q. An, L. Huang, Q. Qian, Y. Jiang, S. Wang, R. Zhang, L. Geng, L. Wang
Insights into in-situ TiB/dual-phase Ti alloy interface and its high load-bearing capacity
J. Mater. Sci. Technol., 119 (2022), pp. 156-166, 10.1016/j.jmst.2021.12.035
View PDFView articleView in ScopusGoogle Scholar
11. [11]
X. Huang, Y. Gao, Y. Yi, P. Xiao, Y. Jian, Y. Wang, S. Zhao, Q. Liu, Z. Ren
Microstructure evolution mechanisms and strength improvement of (6.5 vol%TiC + 3.3 vol%Ti_5Si_3)/Ti6Al4V composites via heat treatments
Mater. Sci. Eng. A., 805 (2021), Article 140581, 10.1016/j.msea.2020.140581
View PDFView articleView in ScopusGoogle Scholar
12. [12]
W.J. Lu, X.L. Guo, J.L. Meng, F.Q. Wang, L.Q. Wang, D. Zhang
Analysis of the coupling effects of TiB whiskers and TiC particles on the fracture toughness of (TiB + TiC)/TC4 composites: experiment and modeling
Metall. Mater. Trans. A-Phys. Metall. Mater. Sci., 46A (8) (2015), pp. 3490-3501, 10.1007/s11661-015-2973-6
View in ScopusGoogle Scholar
13. [13]
H. Liu, J. Han, Y. Han, M. Fang, X. Wang, G. Huang, W. Lu
Formability, densification behavior and hierarchical grain structure of laser-directed energy deposition of TiB reinforced titanium matrix composites
Compos. B Eng. (2023), p. 267, 10.1016/j.compositesb.2023.111039
View in ScopusGoogle Scholar
14. [14]
X. Wang, S. Li, Y. Han, G. Huang, J. Mao, W. Lu
Roles of reinforcements in twin nucleation and nano-α precipitation in the hybrid TiB/TiC-reinforced titanium matrix composites during high-temperature fatigue
Scr. Mater., 196 (2021), Article 113758, 10.1016/j.scriptamat.2021.113758
View PDFView articleView in ScopusGoogle Scholar
15. [15]
P. Qiu, Y. Han, J. Le, G. Huang, L. Lei, L. Xiao, W. Lu
Particulate induced dynamic globularization/recrystallization and unique superplasticity in TiB/near-α Ti matrix composites
Mater. Charact., 167 (2020), 10.1016/j.matchar.2020.110458
Google Scholar
16. [16]
P. Qiu, J. Le, Y. Han, Y. Chen, G. Huang, J. Mao, L. Lei, W. Lu
Superior superplasticity and multiple accommodation mechanisms in TiB reinforced near-α titanium matrix composites
Compos. B Eng. (2022), p. 238, 10.1016/j.compositesb.2022.109940

View in ScopusGoogle Scholar

17. [17]

Z.G. Zhu, X.H. An, W.J. Lu, Z.M. Li, F.L. Ng, X.Z. Liao, U. Ramamurty, S.M.L. Nai, J. Wei

Selective laser melting enabling the hierarchically heterogeneous microstructure and excellent mechanical properties in an interstitial solute strengthened high entropy alloy

Mater Res Lett, 7 (11) (2019), pp. 453-459, 10.1080/21663831.2019.1650131

View in ScopusGoogle Scholar

18. [18]

Z. Li, Q. Kang, Y. Chen, X. Xv, T. Zhou, G. Wang

The microstructure evolution and the effect of grain size, temperature, and TiBw on the deformation mechanism of TiBw/TA15 composites during high temperature deformation

Materials Science and Engineering: A, 878 (2023), p. 145213, 10.1016/j.msea.2023.145213

View PDFView articleView in ScopusGoogle Scholar

19. [19]

G.J. Cao, L. Geng, M. Naka

Elastic properties of titanium monoboride measured by nanoindentation

J. Am. Ceram. Soc., 89 (12) (2006), pp. 3836-3838, 10.1111/j.1551-2916.2006.01280.x

View in ScopusGoogle Scholar

20. [20]

S. Gorsse, Y. Le Petitcorps, S. Matar, F. Rebillat

Investigation of the Young's modulus of TiB needles in situ produced in titanium matrix composite

Mater. Sci. Eng. A., 340 (1–2) (2003), pp. 80-87, 10.1016/S0921-5093(02)00188-0

View PDFView articleView in ScopusGoogle Scholar

21. [21]

K.S.R. Chandran, K.B. Panda, S.S. Sahay

TiBw-reinforced Ti composites: processing, properties, application prospects, and research needs

J. Met., 56 (5) (2004), pp. 42-48, 10.1007/s11837-004-0127-1

Google Scholar

22. [22]

G. Singh, U. Ramamurty

Boron modified titanium alloys

Prog. Mater. Sci., 111 (2020) (2020), Article 100653, 10.1016/j.pmatsci.2020.100653

View PDFView articleView in ScopusGoogle Scholar

23. [23]

W.J. Lu, D. Zhang, X.N. Zhang, R.J. Wu, T. Sakata, H. Mori

Microstructural characterization of TiB in in situ synthesized titanium matrix composites prepared by common casting technique

J. Alloys Compd., 327 (1–2) (2001), pp. 240-247, 10.1016/S0925-8388(01)01445-1

View PDFView articleView in ScopusGoogle Scholar

24. [24]

B.G. Fu, H.W. Wang, C.M. Zou, Z.J. Wei

Microstructural characterization of in situ synthesized TiB in cast Ti-1100-0.10B alloy

Trans. Nonferrous Metals Soc. China, 25 (7) (2015), pp. 2206-2213, 10.1016/S1003-6326(15)63833-X

View PDFView articleView in ScopusGoogle Scholar

25. [25]
W. Zhang, Y. Feng, W. Chen, J. Yang
Effects of heat treatment on the microstructure and mechanical properties of in situ inhomogeneous TiBw/Ti6Al4V composite fabricated by pre–sintering and canned powder extrusion
J. Alloys Compd., 693 (2017), pp. 1116-1123, 10.1016/j.jallcom.2016.09.229
View PDFView articleView in ScopusGoogle Scholar
26. [26]
S.D. Luo, T.T. Song, B. Liu, J. Tian, M. Qian
Recent advances in the design and fabrication of strong and ductile (tensile) titanium metal matrix composites
Adv. Eng. Mater., 21 (7) (2019), Article 1801331, 10.1002/adem.201801331
View in ScopusGoogle Scholar
27. [27]
L. Huang, Q. An, L. Geng, S. Wang, S. Jiang, X. Cui, R. Zhang, F. Sun, Y. Jiao, X. Chen, C. Wang
Multiscale architecture and superior high-temperature performance of discontinuously reinforced titanium matrix composites
Adv. Mater., 33 (6) (2021), pp. 1-28, 10.1002/adma.202000688
Google Scholar
28. [28]
W.H. Yu, S.L. Sing, C.K. Chua, C.N. Kuo, X.L. Tian
Particle-reinforced metal matrix nanocomposites fabricated by selective laser melting: a state of the art review
Prog. Mater. Sci., 104 (2019), pp. 330-379, 10.1016/j.pmatsci.2019.04.006
View PDFView articleView in ScopusGoogle Scholar
29. [29]
K. Morsi, V.V. Patel
Processing and properties of titanium-titanium boride (TiBw) matrix composites - a review
J. Mater. Sci., 42 (6) (2007), pp. 2037-2047, 10.1007/s10853-006-0776-2
View in ScopusGoogle Scholar
30. [30]
L.J. Huang, L. Geng
Discontinuously Reinforced Titanium Matrix Composites_ Microstructure Design and Property Optimization
Springer Nature (2017)
Google Scholar
31. [31]
S.C. Tjong, Y.W. Mai
Processing-structure-property aspects of particulate- and whisker-reinforced titanium matrix composites
Compos. Sci. Technol., 68 (3–4) (2008), pp. 583-601, 10.1016/j.compscitech.2007.07.016
View PDFView articleView in ScopusGoogle Scholar
32. [32]
S. Tamirisakandala, D.B. Miracle
Microstructure engineering of titanium alloys via small boron additions

International Journal of Advances in Engineering Sciences and Applied Mathematics, 2 (4) (2012), pp. 168-180, 10.1007/s12572-011-0033-z
Google Scholar
33. [33]
I. Sen, L. Maheshwari, S. Tamirisakandala, D.B. Miracle, U. Ramamurty
Micromechanisms of damage in a hypereutectic Ti-6Al-4V-B alloy
Mater. Sci. Eng. A., 518 (1–2) (2009), pp. 162-166, 10.1016/j.msea.2009.04.039
View PDFView articleView in ScopusGoogle Scholar
34. [34]
G. Liu, G.J. Zhang, F. Jiang, X.D. Ding, Y.J. Sun, J. Sun, E. Ma
Nanostructured high-strength molybdenum alloys with unprecedented tensile ductility
Nat. Mater., 12 (4) (2013), pp. 344-350, 10.1038/nmat3544
View in ScopusGoogle Scholar
35. [35]
Q. Li, S. Huang, Y.K. Zhao, Y.M. Gao, U. Ramamurty
Simultaneous enhancements of strength, ductility, and toughness in a TiB reinforced titanium matrix composite
Acta Mater., 254 (2023), Article 118995, 10.1016/j.actamat.2023.118995
View PDFView articleView in ScopusGoogle Scholar
36. [36]
M. Peters, J. Kumpfert, C.H. Ward, C. Leyens
Titanium alloys for aerospace applications
Adv. Eng. Mater., 5 (6) (2003), pp. 419-427, 10.1002/adem.200310095
View in ScopusGoogle Scholar
37. [37]
M. Peters, C. Leyens
Titanium and Titanium Alloys: Fundamentals and Applications
John Wiley and Sons, New York (2006)
Google Scholar
38. [38]
C.X. Cui, B.M. Hu, L.C. Zhao, S.J. Liu
Titanium alloy production technology, market prospects and industry development
Mater. Des., 32 (3) (2011), pp. 1684-1691, 10.1016/j.matdes.2010.09.011
View PDFView articleView in ScopusGoogle Scholar
39. [39]
T.K. Mitsuo Niinomi
Toughness and strength of microstructurally controlled titanium alloys
ISIJ Int., 31 (8) (1991), pp. 848-855, 10.2355/isijinternational.31.848
Google Scholar
40. [40]
D. Banerjee, J.C. Williams
Perspectives on titanium science and technology
Acta Mater., 61 (3) (2013), pp. 844-879, 10.1016/j.actamat.2012.10.043
View PDFView articleView in ScopusGoogle Scholar

41. [41]
G. Lutjering
Influence of processing on microstructure and mechanical properties of (α+β) titanium alloys
Mat Sci Eng a-Struct., 243 (1–2) (1998), pp. 32-45, 10.1016/S0921-5093(97)00778-8
View PDFView articleView in ScopusGoogle Scholar
42. [42]
M. Niinomi, T. Kobayashi
Fracture characteristics analysis related to the microstructures in titanium alloys
Mater. Sci. Eng. A., 213 (1–2) (1996), pp. 16-24, 10.1016/0921-5093(96)10239-2
View PDFView articleView in ScopusGoogle Scholar
43. [43]
J. Kang, H.S. Oh, S. Wei, G. Zhu, I. Nakahata, C.C. Tasan
An in situ study of microstructural strain localization and damage evolution in an (α+β) Ti-Al-V-Fe-Si-O alloy
Acta Mater., 242 (2023), 10.1016/j.actamat.2022.118424
Google Scholar
44. [44]
S.X. Huang, Q.Y. Zhao, C. Lin, C. Wu, Y.Q. Zhao, W.J. Jia, C.L. Mao
In-situ investigation of tensile behaviors of Ti-6Al alloy with extra low interstitial
Mater. Sci. Eng. A., 809 (2021), Article 140958, 10.1016/j.msea.2021.140958
View PDFView articleView in ScopusGoogle Scholar
45. [45]
D.R. Chichili, K.T. Ramesh, K.J. Hemker
The high-strain-rate response of alpha-titanium: experiments, deformation mechanisms and modeling
Acta Mater., 46 (3) (1998), pp. 1025-1043, 10.1016/S1359-6454(97)00287-5
View PDFView articleView in ScopusGoogle Scholar
46. [46]
Z. Zheng, S. Waheed, D.S. Balint, F.P.E. Dunne
Slip transfer across phase boundaries in dual phase titanium alloys and the effect on strain rate sensitivity
Int. J. Plast., 104 (2018), pp. 23-38, 10.1016/j.ijplas.2018.01.011
View PDFView articleGoogle Scholar
47. [47]
W. Zhong, K. Yu, J. Shi, Y. Shen, P. Li, L. Jinzhong
High-temperature oxidation behavior of TA15 aerospace titanium alloy at 500 °C and 800 °C
J. Mater. Res. Technol., 30 (2024), pp. 3355-3366, 10.1016/j.jmrt.2024.04.072
View PDFView articleView in ScopusGoogle Scholar
48. [48]
Y. Feng, G. Cui, W. Zhang, W. Chen, Y. Yu
High temperature tensile fracture characteristics of the oriented TiB whisker reinforced TA15 matrix composites fabricated by pre-sintering and canned extrusion
J. Alloys Compd., 738 (2018), pp. 164-172, 10.1016/j.jallcom.2017.12.132
View PDFView articleView in ScopusGoogle Scholar

49. [49]
L. Zhu, Y. Pan, Y. Liu, Z. Sun, X. Wang, H. Nan, M.-A. Mughal, D. Lu, X. Lu
Effects of microstructure characteristics on the tensile properties and fracture toughness of TA15 alloy fabricated by hot isostatic pressing
Int. J. Miner. Metall. Mater., 30 (4) (2023), pp. 697-706, 10.1007/s12613-021-2371-6
Google Scholar
50. [50]
Z. Sun, H. Yang
Microstructure and mechanical properties of TA15 titanium alloy under multi-step local loading forming
Materials Science and Engineering: A., 523 (1–2) (2009), pp. 184-192, 10.1016/j.msea.2009.05.058
View PDFView articleView in ScopusGoogle Scholar
51. [51]
S. Wang, L. Huang, S. Jiang, R. Zhang, B. Liu, F. Sun, Q. An, Y. Jiao, L. Geng
Microstructure evolution and tensile properties of as-rolled TiB/TA15 composites with network microstructure
Materials Science and Engineering: A, 804 (2021), 10.1016/j.msea.2021.140783
Google Scholar
52. [52]
S. Huang, R.L. Narayan, J.H.K. Tan, S.L. Sing, W.Y. Yeong
Resolving the porosity-unmelted inclusion dilemma during in-situ alloying of Ti34Nb via laser powder bed fusion
Acta Mater., 204 (2021), 10.1016/j.actamat.2020.116522
Google Scholar
53. [53]
S. Huang, P. Kumar, W.Y. Yeong, R.L. Narayan, U. Ramamurty
Fracture behavior of laser powder bed fusion fabricated Ti41Nb via in-situ alloying
Acta Mater., 225 (2022), Article 117593, 10.1016/j.actamat.2021.117593
View PDFView articleView in ScopusGoogle Scholar
54. [54]
S. Huang, S.L. Sing, G. de Looze, R. Wilson, W.Y. Yeong
Laser powder bed fusion of titanium-tantalum alloys: compositions and designs for biomedical applications
J. Mech. Behav. Biomed. Mater., 108 (2020), Article 103775, 10.1016/j.jmbbm.2020.103775
View PDFView articleView in ScopusGoogle Scholar
55. [55]
A.E. Davis, J. Donoghue, J.R. Kennedy, N. Byres, P.B. Prangnell
In-situ observation of single variant alpha colony formation in Ti-6Al-4V
Acta Mater., 220 (2021), 10.1016/j.actamat.2021.117315
Google Scholar
56. [56]
J. Tiley, T. Searles, E. Lee, S. Kar, R. Banerjee, J.C. Russ, H.L. Fraser
Quantification of microstructural features in α/β titanium alloys
Materials Science and Engineering: A., 372 (1–2) (2004), pp. 191-198, 10.1016/j.msea.2003.12.008

View PDFView articleView in ScopusGoogle Scholar

57. [57]

M. Humbert, N. Gey

The calculation of a parent grain orientation from inherited variants for approximate (b.c.c.–h.c.p.) orientation relations

J. Appl. Crystallogr., 35 (4) (2002), pp. 401-405, 10.1107/s0021889802005824

View in ScopusGoogle Scholar

58. [58]

S.Y. Wei, P. Kumar, K.B. Lau, D. Wuu, L.L. Liew, F.X. Wei, S.L. Teo, A. Cheong, C.K. Ng, B.C. Zhang, C.C. Tan, P. Wang, U. Ramamurty

Effect of heat treatment on the microstructure and mechanical properties of 2.4 GPa grade maraging steel fabricated by laser powder bed fusion

Addit. Manuf., 59 (2022), 10.1016/j.addma.2022.103190

Google Scholar

59. [59]

J. Radhakrishnan, P. Kumar, S.S. Gan, A. Bryl, J. McKinnell, U. Ramamurty

Microstructure and tensile properties of binder jet printed 17–4 precipitation hardened martensitic stainless steel

Materials Science and Engineering: A., 860 (2022), 10.1016/j.msea.2022.144270

Google Scholar

60. [60]

S.-H. Li, D.-H. Lee, Y. Zhao, U. Ramamurty

Hydrogen-induced softening and embrittlement in 316L stainless steel fabricated using laser-powder bed fusion

Acta Mater, 274 (2024), p. 119959, 10.1016/j.actamat.2024.119959

View PDFView articleView in ScopusGoogle Scholar

61. [61]

ASTM E8M-22

Standard Test Methods for Tension Testing of Metallic Materials

ASTM International, West Conshohocken (2022)

Google Scholar

62. [62]

ASTM E399-20a

Standard Test Method for Linear-Elastic Plane-Strain Fracture Toughness of Metallic Materials

ASTM International, West Conshohocken (2022)

Google Scholar

63. [63]

ASTM E647-15

Standard Test Method for Measurement of Fatigue Crack Growth Rates

ASTM International, West Conshohocken (2016)

Google Scholar

64. [64]

P. Kumar, O. Prakash, U. Ramamurty

Micro-and meso-structures and their influence on mechanical properties of selectively laser melted

Ti-6Al-4V
Acta Mater., 154 (2018), pp. 246-260, 10.1016/j.actamat.2018.05.044
View PDFView articleView in ScopusGoogle Scholar
65. [65]
J. Radhakrishnan, P. Kumar, S.S. Gan, A. Bryl, J. McKinnell, U. Ramamurty
Fatigue resistance of the binder jet printed 17-4 precipitation hardened martensitic stainless steel
Materials Science and Engineering: A., 865 (2023), 10.1016/j.msea.2022.144451
Google Scholar
66. [66]
Q. Li, Y. Chen, X.Y. Huang, Y.R. Wang, Y.K. Zhao, U. Ramamurty, Y.M. Gao
Long-whisker type TiB phase introduced by micron-sized precursors and its prominent strengthening effect in titanium matrix composites
Mater. Sci. Eng. A., 841 (2022), Article 143021, 10.1016/j.msea.2022.143021
View PDFView articleView in ScopusGoogle Scholar
67. [67]
D. Wang, H. Li, X. Wang, W. Zheng, Z. Lin, G. Liu
The microstructure evolution and mechanical properties of TiBw/TA15 composite with network structure prepared by rapid current assisted sintering
Metals-Basel, 9 (5) (2019), 10.3390/met9050540
Google Scholar
68. [68]
S. Li, S. Li, L. Liu, L. Gao, Y. Fu, X. Zhang, B. Li
High temperature softening mechanism of powder metallurgy TA15 alloy
Materials Science and Engineering: A, 877 (2023), 10.1016/j.msea.2023.145160
Google Scholar
69. [69]
J.R. Seal, M.A. Crimp, T.R. Bieler, C.J. Boehlert
Analysis of slip transfer and deformation behavior across the α/β interface in Ti–5Al–2.5Sn (wt.%) with an equiaxed microstructure
Materials Science and Engineering: A., 552 (2012), pp. 61-68, 10.1016/j.msea.2012.04.114
View PDFView articleView in ScopusGoogle Scholar
70. [70]
S. Wei, L. Huang, X. Li, Y. Jiao, W. Ren, L. Geng
Network-Strengthened Ti-6Al-4V/(TiC+TiB) composites: powder metallurgy processing and enhanced tensile properties at elevated temperatures
Metall. Mater. Trans. A, 50 (8) (2019), pp. 3629-3645, 10.1007/s11661-019-05244-7
View in ScopusGoogle Scholar
71. [71]
L.J. Huang, L. Geng, B. Wang, L.Z. Wu
Effects of volume fraction on the microstructure and tensile properties of in situ TiBw/Ti6Al4V composites with novel network microstructure
Mater. Des., 45 (2013), pp. 532-538, 10.1016/j.matdes.2012.09.043
View PDFView articleView in ScopusGoogle Scholar
72. [72]

X. Chen, L. Huang, J. Song, S. Zhou, S. Wang, R. Zhang, L. Geng
Towards strength-ductility synergy of titanium matrix composites through configuration design: mesoscale deformation and damage behaviors
Compos. B Eng. (2024), p. 283, 10.1016/j.compositesb.2024.111651
Google Scholar

73. [73]
L. Shikai, X. Baiqing, H. Songxiao
Effects of cooling rate on the fracture properties of TA15 ELI alloy plates
Rare Met., 26 (1) (2007), pp. 33-38, 10.1016/s1001-0521(07)60024-2
View PDFView articleView in ScopusGoogle Scholar

74. [74]
D. Hill, R. Banerjee, D. Huber, J. Tiley, H.L. Fraser
Formation of equiaxed alpha in TiB reinforced Ti alloy composites
Scr. Mater., 52 (5) (2005), pp. 387-392, 10.1016/j.scriptamat.2004.10.019
View PDFView articleView in ScopusGoogle Scholar

75. [75]
J. Le, C.J. Boehlert, G.F. Huang, J.W. Mao, L.M. Lei, Y.F. Han, W.J. Lu
TiB whisker induced variant selection in titanium matrix composites
Scr. Mater., 217 (2022), Article 114772, 10.1016/j.scriptamat.2022.114772
View PDFView articleView in ScopusGoogle Scholar

76. [76]
S. Tamirisakandala, R.B. Bhat, J.S. Tiley, D.B. Miracle
Grain refinement of cast titanium alloys via trace boron addition
Scr. Mater., 53 (12) (2005), pp. 1421-1426, 10.1016/j.scriptamat.2005.08.020
View PDFView articleView in ScopusGoogle Scholar

77. [77]
B. Wang, L.J. Huang, L. Geng, Z.S. Yu
Modification of microstructure and tensile property of TiBw/near-α Ti composites by tailoring TiBw distribution and heat treatment
J. Alloys Compd., 690 (2017), pp. 424-430, 10.1016/j.jallcom.2016.08.138
View PDFView articleView in ScopusGoogle Scholar

78. [78]
A. Venkataraman, P.A. Shade, R. Adebisi, S. Sathish, A.L. Pilchak, G.B. Viswanathan, M.C. Brandes, M.J. Mills, M.D. Sangid
Study of structure and deformation pathways in Ti-7Al using atomistic simulations, experiments, and characterization
Metall. Mater. Trans. A, 48 (5) (2017), pp. 2222-2236, 10.1007/s11661-017-4024-y
View in ScopusGoogle Scholar

79. [79]
Z. Li, Y. Chen, Q. Kang, X. Xv, T. Zhou, G. Wang
Differences in mechanical properties and high temperature deformation behavior between TiBw/Ti65 and TiBw/TA15 composites with network structure
J. Mater. Res. Technol., 26 (2023), pp. 9169-9189, 10.1016/j.jmrt.2023.09.216
View PDFView articleView in ScopusGoogle Scholar

80. [80]
Z. Li, Q. Kang, G. Wang, X. Sui, Y. Liu, S. Luo
Microstructure evolution during hot-packed rolling and mechanical properties anisotropy of as-rolled network-structured TiBw/TA15 composites
Materials Science and Engineering: A, 849 (2022), 10.1016/j.msea.2022.143518
Google Scholar
81. [81]
R. Zhang, S. Wang, W. Lu, F. Sun, L. Huang, L. Bolzoni, L. Geng, F. Yang
Enhancing microstructure refinement and strengthening efficiency of TiBw/near α-Ti composites by combining solid-solution treatment with hot processing
Compos. B Eng. (2023), p. 257, 10.1016/j.compositesb.2023.110696
Google Scholar
82. [82]
P. Kumar, U. Ramamurty
Microstructural optimization through heat treatment for enhancing the fracture toughness and fatigue crack growth resistance of selective laser melted Ti-6Al-4V alloy
Acta Mater., 169 (2019), pp. 45-59, 10.1016/j.actamat.2019.03.003
View PDFView articleGoogle Scholar
83. [83]
I. Sen, K. Gopinath, R. Datta, U. Ramamurty
Fatigue in Ti-6Al-4V-B alloys
Acta Mater., 58 (20) (2010), pp. 6799-6809, 10.1016/j.actamat.2010.09.008
View PDFView articleView in ScopusGoogle Scholar
84. [84]
J.R. Weertman
Rate of growth of fatigue cracks calculated from the theory of infinitesimal dislocations distributed on a plane
Int. J. Fract. Mech., 2 (1966), pp. 460-467, 10.1007/BF00183823
View in ScopusGoogle Scholar
85. [85]
R.J. R.
Mechanics of Crack Tip Deformation and Extension by Fatigue, Fatigue Crack Propagation
(1967), pp. 247-311, 10.1520/STP47234S
Google Scholar
86. [86]
S. Suresh
Fatigue of Materials
Cambridge University Press, Cambridge (2012)
Google Scholar
87. [87]
R.O. Ritchie
The conflicts between strength and toughness
Nat. Mater., 10 (2011), pp. 817-822, 10.1038/nmat3115
View in ScopusGoogle Scholar

88. [88]
M.J. Paul, J.J. Kruzic, U. Ramamurty, B. Gludovatz
The importance of fracture toughness evaluation for additively manufactured metals
Acta Mater. (2024), 10.1016/j.actamat.2024.120061
Google Scholar
89. [89]
V.M. Imayev, R.A. Gaisin, R.M. Imayev
Effect of boron additions and processing on microstructure and mechanical properties of a titanium alloy Ti–6.5Al–3.3Mo–0.3Si
Materials Science and Engineering: A, 641 (2015), pp. 71-83, 10.1016/j.msea.2015.06.033
View PDFView articleView in ScopusGoogle Scholar
90. [90]
R. Sarkar, P. Ghosal, T.K. Nandy, K.K. Ray
Structure–property correlation of a boron and carbon modified as cast β titanium alloy
Philos. Mag. A, 93 (15) (2013), pp. 1936-1957, 10.1080/14786435.2013.765979
View in ScopusGoogle Scholar
91. [91]
K. Prasad, R. Sarkar, S.V. Kamat, T.K. Nandy
Fracture toughness and low cycle fatigue behaviour in boron modified Timetal 834 titanium alloy
Materials Science and Engineering: A, 529 (2011), pp. 74-80, 10.1016/j.msea.2011.08.062
View PDFView articleView in ScopusGoogle Scholar
92. [92]
V.K. Chandravanshi, A. Bhattacharjee, S.V. Kamat, T.K. Nandy
Influence of thermomechanical processing and heat treatment on microstructure, tensile properties and fracture toughness of Ti-1100-0.1B alloy
J. Alloys Compd., 589 (2014), pp. 336-345, 10.1016/j.jallcom.2013.11.014
View PDFView articleView in ScopusGoogle Scholar
93. [93]
M.J. Paul, Q. Liu, J.P. Best, X. Li, J.J. Kruzic, U. Ramamurty, B. Gludovatz
Fracture resistance of AlSi10Mg fabricated by laser powder bed fusion
Acta Mater., 211 (2021), 10.1016/j.actamat.2021.116869
Google Scholar
94. [94]
R.O. Ritchie
Toughening materials: enhancing resistance to fracture
Philosophical Transactions of the Royal Society A, 379 (2203) (2021), Article 20200437, 10.1098/rsta.2020.0437
View in ScopusGoogle Scholar
95. [95]
S. Huang, P. Kumar, C.W.J. Lim, J. Radhakrishnan, U. Ramamurty
Fracture behavior of PH15-5 stainless steel manufactured via directed energy deposition
Mater. Des. (2023), p. 235, 10.1016/j.matdes.2023.112421
View in ScopusGoogle Scholar
96. [96]

R.O. Ritchie, J.F. Knott, J.R. Rice
On the relationship between critical tensile stress and fracture toughness in mild steel
J. Mech. Phys. Solid., 21 (6) (1973), pp. 395-410, 10.1016/0022-5096(73)90008-2
View PDFView articleView in ScopusGoogle Scholar

97. [97]
R.O. Ritchie, W.L. Server, R.A. Wullaert
Critical fracture-stress and fracture strain models for the prediction of lower and upper shelf toughness in nuclear pressure-vessel steels
Metall. Trans. A, 10 (10) (1979), pp. 1557-1570, 10.1007/Bf02812022
View in ScopusGoogle Scholar

98. [98]
J. Chen, H. Yin, Q. Sun
Effects of grain size on fatigue crack growth behaviors of nanocrystalline superelastic NiTi shape memory alloys
Acta Mater., 195 (2020), pp. 141-150, 10.1016/j.actamat.2020.05.008
View PDFView articleView in ScopusGoogle Scholar

99. [99]
T.H. Becker, P. Kumar, U. Ramamurty
Fracture and fatigue in additively manufactured metals
Acta Mater., 219 (2021), 10.1016/j.actamat.2021.117240
Google Scholar

100. [100]
S.S. Youssef, X. Zheng, M. Qi, Y. Ma, S. Huang, J. Qiu, S. Zheng, J. Lei, R. Yang
Effects of Al content and α2 precipitation on the fatigue crack growth behaviors of binary Ti–Al alloys
Materials Science and Engineering: A., 819 (2021), 10.1016/j.msea.2021.141513
Google Scholar

101. [101]
J.Q. Ren, Q. Wang, B.B. Zhang, D. Yang, X.F. Lu, X.B. Zhang, X.D. Zhang, J.Y. Hu
Influence of microstructure on fatigue crack growth behavior of Ti-6Al-3Nb-2Zr-1Mo alloy: bimodal vs. lamellar structures
Intermetallics, 130 (2021), Article 107058, 10.1016/j.intermet.2020.107058
View PDFView articleView in ScopusGoogle Scholar